

1 **A weather regime characterisation of winter biomass aerosol transport from southern Africa**

2

3 Marco Gaetani (1,2); Benjamin Pohl (3); Maria del Carmen Alvarez Castro (4,5); Cyrille Flamant (6);

4 Paola Formenti (1)

5

6 (1) Université de Paris and Université Paris Est Creteil, CNRS, LISA, F-75013 Paris, France

7 (2) Scuola Universitaria Superiore IUSS, Pavia, Italia

8 (3) CRC/Biogéosciences, UMR6282 CNRS / Université de Bourgogne Franche-Comté, Dijon, France

9 (4) University Pablo de Olavide, Seville, Spain

10 (5) CMCC, Bologna, Italy

11 (6) Institut Pierre Simon Laplace, Laboratoire Atmosphères, Milieux, Observations Spatiales, UMR

12 CNRS 8190, Sorbonne Université, Université Versailles Saint Quentin, Paris, France

13

14 Contact: marco.gaetani@iusspavia.it

15 **Abstract**

16 During austral winter, a compact low cloud deck over the South Atlantic contrasts with clear sky over
17 southern Africa, where forest fires triggered by dry conditions emit large amount of biomass burning
18 aerosols (BBA) in the free troposphere. Most of the BBA burden crosses the South Atlantic
19 embedded in the tropical easterly flow. However, midlatitude synoptic disturbances can deflect part
20 of the aerosol from the main transport path towards southern extratropics.

21 In this study, the first objective classification of the synoptic variability controlling the spatial
22 distribution of BBA in southern Africa and the South Atlantic during austral winter (August to
23 October) is presented. By analysing atmospheric circulation data from reanalysis products, a 6-class
24 weather regime (WR) classification of the region is constructed. The classification reveals that the
25 synoptic variability is composed of four WRs representing disturbances travelling at midlatitudes,
26 and two WRs accounting for pressure anomalies in the South Atlantic. The WR classification is then
27 successfully used to characterise the aerosol spatial distribution in the region in the period 2003-
28 2017, in both reanalysis products and station data. Results show that the BBA transport towards
29 southern extratropics is controlled by weather regimes associated with midlatitude synoptic
30 disturbances. In particular, depending on the relative position of the pressure anomalies along the
31 midlatitude westerly flow, the BBA transport is deflected from the main tropical route towards
32 southern Africa or the South Atlantic. Moreover, the WRs accounting for midlatitude disturbances
33 show organised transition sequences, which allow to illustrate the evolution of the BBA northerly
34 transport across the region in the context of a wave pattern.

35 The skill in characterising the BBA transport shown by the WR classification indicates the potential
36 for using it as a diagnostic/predictive tool for the aerosol dynamics, which is a key component for
37 the full understanding and modelling of the complex radiation-aerosol-cloud interactions controlling
38 the atmospheric radiative budget in the region.

39 1. Introduction

40 Natural and anthropogenic tropospheric aerosols are fundamental ingredients of the climate system.
41 They influence the radiative properties of the atmosphere by deflecting and absorbing radiation
42 (direct effect) and the cloud formation and properties by absorption (semi-direct effect) as well as by
43 acting as cloud condensation nuclei (indirect effect). As a consequence, aerosols can influence the
44 atmospheric and climate dynamics (Bellouin et al., 2020).

45 Africa is the Earth's largest source of biomass burning aerosol (BBA; e.g. van der Werf et al., 2010,
46 2017). The transport of BBA, originating from central Africa and embedded in the tropical
47 midtropospheric easterly flow, occurs mostly above the Atlantic Ocean (Fig. 1a), and is a prominent
48 feature during austral winter (June to October; Fig. 1b) between the Equator and 20°S, when dry
49 conditions in central Africa favour the development of forest fires (Horowitz et al., 2017). However,
50 extratropical rivers of smoke are also observed to extend to 30-40°S between August and October
51 (Fig. 1b). The term 'river of smoke' refers to the sharply defined boundaries of the smoke plume,
52 which can be several hundred kilometres wide and flow over a few thousands kilometres above
53 southern Africa towards Southern and Indian Oceans (McMillan et al., 2003; Swap et al., 2003).
54 Depending on the transport path (e.g. either above the continent or recirculated above the ocean),
55 physical and chemical properties of the BBA may change (Abel et al., 2003; Eck et al., 2003; Formenti
56 et al., 2003; Haywood et al., 2003; Pistone et al., 2019; Wu et al., 2020). The characterisation of BBA
57 transport in terms of synoptic atmospheric circulation is therefore one of the key elements to shed
58 light on the already complex picture of the radiation-aerosol-cloud interactions (Adebisi and
59 Zuidema, 2018; Formenti et al., 2019; Haywood et al., 2003, 2021; Lindesay et al., 1996; Mallet et al.,
60 2020; Redemann et al., 2021; Swap et al., 2003; Zuidema et al., 2016). Additionally, the extent and
61 direction of BBA transport may condition the atmospheric remote supply of nutrients and pollutants
62 to the South Atlantic, the Southern Ocean, and the Indian Ocean, as well as to Antarctica (Baker et
63 al., 2010; Barkley et al., 2019; Gao et al., 2003, 2020; Swap et al., 1996; Wai et al., 2014).

64 Understanding the role of the radiation-aerosol-cloud interaction in controlling the atmospheric
65 radiative budget and, consequently, climate dynamics is a key aspect for the improvement of climate
66 modelling. Indeed, even state-of-the art climate models still struggle in reliably representing the
67 atmospheric radiative forcing, due to inaccurate parametrizations of the radiation-aerosol-cloud
68 interaction (Mallet et al., 2020; Stier et al., 2013; Tang et al., 2019). This is particularly relevant in the
69 South Atlantic, where the incomplete knowledge of the smoke-cloud regime generates large
70 discrepancies in the modelling of radiative forcing and sea surface temperature (SST) in the region,
71 eventually affecting climate simulations at regional and global scale (Zuidema et al., 2016). While a
72 conceptual understanding of the meteorological conditions determining the transport of aerosols

73 and pollutants at the subcontinental scale exists (Diab et al., 1996; Garstang et al., 1996; Tyson,
74 1997), the large-scale drivers of the aerosol spatial distribution in the region are still not understood
75 and an objective synoptic characterisation of the wintertime BBA transport is still missing to date.
76 Indeed, synoptic circulation in the southern Africa/South Atlantic sector is discussed in literature
77 mainly in relationship with convection and precipitation during austral summer (e.g. Crétat et al.,
78 2019; Dieppois et al., 2016; Fauchereau et al., 2009; Macron et al., 2014; Pohl et al., 2018; Vignaud et
79 al., 2012).

80 The scope of this paper is to fill the gaps in the understanding of atmospheric and aerosol dynamics
81 during austral winter in the southern Africa/South Atlantic sector, by providing a characterisation of
82 the synoptic variability of the atmospheric circulation, and determining the circulation patterns
83 controlling the transport of BBA from the tropics to the extratropics. To this aim, an objective
84 weather regime (WR) classification of the winter atmospheric circulation in the southern
85 Africa/South Atlantic sector is presented for the first time, and used to characterise the BBA
86 transport in the region. In particular, the study focuses on the characterisation of the southward
87 deflection of BBA from the mean tropical easterly flow from August to October (ASO) in the period
88 2003-2017. Atmospheric circulation data from a reanalysis product are first used to classify the
89 synoptic circulation patterns. Then, the classification is used to characterise the BBA transport
90 anomalies in reanalysis data and in situ observations in the region. The paper is organised as follows:
91 in Section 2, data and methods used in the analysis are presented; in Section 3, the WR classification
92 is presented and the synoptic characterisation of BBA anomalies is discussed; conclusions and
93 perspectives are summarised in Section 4.

94 **2. Data and Methods**

95 **2.1. Reanalysis and gridded observations**

96 The atmospheric circulation and the spatial distribution and optical properties of the BBA over
97 southern Africa and the South Atlantic in ASO 2003-2017 are analysed using data from the
98 Copernicus Atmospheric Monitoring Service reanalysis product (CAMS; Flemming et al., 2017) at 6h
99 time steps (00:00, 06:00, 12:00, and 18:00) and 0.75° horizontal resolution. The BBA emission is
100 estimated by the organic matter mixing ratio at 10m, the BBA transport is estimated as the product
101 of organic matter mixing ratio and wind at 700 hPa, and the aerosol spatial distribution is
102 represented by the aerosol optical depth (AOD) at 550 nm (Fig. 2a). Data from the fifth generation
103 ECMWF reanalysis (ERA5; Hersbach et al., 2020), available at hourly time steps and 0.25° horizontal
104 resolution, are used to validate the WR classification on a longer time period (1981-2020). ERA5 data
105 are selected at 6h time steps (00:00, 06:00, 12:00, and 18:00) and regridded to the CAMS product

106 grid at 0.75°. For both the reanalysis products, daily values are obtained at each grid point as the
107 average of 6h time steps, and daily anomalies are computed by removing the low frequency (LF)
108 component of the time series, estimated by computing monthly means from daily data and
109 interpolating them to daily time steps using a cubic spline interpolation. The limited coverage of the
110 CAMS reanalysis (15 years) does not allow a robust definition of the climatological seasonal cycle,
111 which would be too dependent on the interannual variability. Therefore, in order to isolate the
112 synoptic variability alone, the definition of a LF component, accounting for the seasonal cycle and
113 the interannual variability, is preferred and applied to both the reanalysis products.

114 Global reconstructions of the observed sea surface temperature (SST) are used to investigate the
115 teleconnections controlling the synoptic variability. Data are extracted from the Met Office Hadley
116 Centre HadISST dataset (Rayner et al., 2003), available from 1871 at monthly time scale and 1°
117 horizontal resolution, and from the NOAA Extended Reconstructed Sea Surface Temperature (ERSST)
118 Version 5 dataset (Huang et al., 2017), available from 1854 at monthly time scale and 2° horizontal
119 resolution.

120 **2.2. In situ aerosol observations**

121 Observed daily values of the AOD at 500 nm from AERONET stations (<https://aeronet.gsfc.nasa.gov/>)
122 are used to validate the synoptic characterisation performed on CAMS data. Stations are selected
123 among the ones with at least 2 years of level 2 data obtained from the Version 3 Direct Sun
124 algorithm (Giles et al., 2018). Stations are selected outside the source region in tropical Africa,
125 namely south of 20°S and west of 10°E (Fig. 2a, Table 1), in order to focus on BBA transport only, not
126 being influenced by the BBA emission which is assumed not to be directly related to synoptic
127 conditions. Among the available stations, St. Helena [15.9°S, 5.7°W] and Wits University [26.2°S,
128 28.0°E] are not included because of the limited coverage (less than 100 observations during the
129 study period). Moreover, the stations closer to the greater Johannesburg and Pretoria urban areas
130 (namely, Durban UKZN [29.8°S, 30.9°E], Pretoria CSIR-DPSS [25.8°S, 28.3°E] and Skukuza [25.0°S,
131 31.2°E]) are not included, because too affected by the proximity of urban sources (Fig. 2a). Three
132 Namibian stations, namely Gobabeb, Henties Bay and HESS, are located very close to each other, in
133 comparison with the size of the rivers of smoke affecting western Namibia (see Fig. 2a). Therefore,
134 the combination of the AOD observations in the three stations would be more representative of
135 regional conditions and filter out local effects on the AOD measurements. Indeed, Henties Bay is a
136 coastal site, exposed to both marine and mineral dust aerosols; Gobabeb is in the Namib Desert,
137 exposed to mineral dust aerosols; HESS is located inland in the savannahs, exposed to possible local
138 sources of BBA. A daily time series associated with the three stations (referred as Namibian Stations,
139 NS) is built by computing the average AOD when observations are available in at least 2 stations out

140 of 3, leading to a time series longer than the three individual time series (276 observations, spanning
141 from 2013 to 2017, see Table 1).

142 For each station, daily AOD anomalies are computed by removing the LF component of the time
143 series, accounting for both the seasonal cycle and the interannual variability, as described in Section
144 2.1. However, the sparseness of the AERONET observations makes difficult the definition of a daily
145 LF component. Therefore, CAMS AOD at 550 nm is selected in an area defined by the grid point the
146 closest to the station coordinates and the adjacent grid points, and averaged to estimate the daily LF
147 component of the AOD at 500 nm. Empirical evidence shows that a quadratic relationship exists
148 between the natural logarithm of AOD and wavelength (Eck et al., 1999). However, at such close
149 wavelengths the relationship can be assumed to be linear, and the relationship between the natural
150 logarithm of AOD at 500 and 550 nm can be modelled as follows:

$$151 \quad \log AOD_{500nm} = a \log AOD_{550nm} + b.$$

152 At each AERONET station, the logarithm of observed and CAMS AOD well correlates during ASO
153 2003-2017 (correlations coefficients lie between 0.71 and 0.90, all significant at 99% level of
154 confidence, see Fig. 3). Therefore, the daily LF component of the observed AOD is estimated by
155 means of a linear regression onto the CAMS LF component. In order to minimise the effect of
156 possible large discrepancies between AERONET and CAMS data, the difference between AERONET
157 and CAMS AOD is computed and the values in the lowest and highest 5% are discarded before the
158 linear regression is performed (the coefficients used in the regression model at each station are
159 displayed in Fig. 3).

160 **2.3. Weather regime classification**

161 The WR classification is performed on the geopotential height at 700 hPa, which is the level where
162 BBA transport is maximal, in the domain [20°W-40°E, Eq-40°S] (see Fig. 2bc). The selection of the
163 domain is made to include the main BBA transport routes in the tropical belt and towards the
164 extratropics. However, during the dry season the synoptic variability in the tropics is reduced in
165 comparison with the extratropics (Baldwin, 2001). Therefore, the southern border of the domain is
166 set to 40°S, not to let the dominant midlatitude modes mask variability in the tropical belt. The
167 atmospheric circulation is first characterised by isolating the main modes of variability represented
168 by the empirical orthogonal functions (EOFs) derived from a principal component analysis (PCA) of
169 the geopotential height daily anomalies. Each mode is represented by a spatial anomaly pattern and
170 a standardized time series (namely, the principal components, PCs) accounting for the amplitude of
171 the anomaly pattern (for more details on PCA, see Storch and Zwiers, 1999). The first 4 EOFs,
172 accounting for at least 80% of the total variance (Fig. S1), are used to classify the WRs by means of a

173 k-means algorithm, using $k = [2, 10]$ (Michelangeli et al., 1995). For each k , the classification is
174 performed 100 times, to ensure reproducibility of the results. A red-noise test is performed to assess
175 the significance of the class partition (Michelangeli et al., 1995), resulting in 6 and 7 classes (Fig. S3).
176 The synoptic characterisation of the BBA transport is performed by using both the 6-class and the 7-
177 class partitions. This study focuses on the 6-class partition, i.e. the classification with the lowest
178 significant number of WRs, which leads to physically coherent atmospheric patterns describing the
179 main features of the synoptic variability (see Section 3.1). Furthermore, the comparison between the
180 6 and 7 class partitions shows that the 6 WR classification performs better in characterising the BBA
181 transport in the region (see Section S3). The robustness of the 6-class partition is tested against
182 different choices of time period (1981-2020), geographical domain ($[20^{\circ}\text{W}-40^{\circ}\text{E}, 10^{\circ}\text{S}-50^{\circ}\text{S}]$) and
183 retained variance (at least 90%, accounted for by the first 7 PCs).

184 **2.4. Aerosol synoptic characterisation**

185 The WR classification is used to characterise the observed AOD data from the AERONET stations in
186 the region (Table 1). Two approaches are used:

187 1) Daily AOD anomalies are linked to the corresponding WR and grouped, and statistical differences
188 among groups are investigated (circulation-to-environment approach, C2E). The significance of the
189 C2E characterisation is assessed by a one-way analysis of variance (ANOVA) with the null hypothesis
190 that the distributions associated with each WR are derived from populations with the same mean.
191 Furthermore, for each WR the significance of the associated AOD anomalies with the respect of the
192 full sample is assessed by a non-parametric Kolmogorov-Smirnov (KS) test.

193 2) Daily AOD anomalies are divided into quartiles, and the changes in the WR occurrences within
194 each quartile are studied (environment-to-circulation approach, E2C). The significance of the E2C
195 characterisation is assessed by computing the chi-squared statistics for each quartile, with the null
196 hypothesis that the associated WR frequencies are derived from the same distribution of the full
197 sample. The chi-squared statistics is tested against the critical value for 5 degrees of freedom and at
198 the 95% level of confidence. The degrees of freedom are estimated as the number of the
199 observation categories (6 WRs) minus the parameters of the distribution to be fitted (the mean WR
200 occurrence, i.e. 1).

201 **3. Results**

202 **3.1. Synoptic characterisation of the regional atmospheric variability**

203 The mean atmospheric conditions over the South Atlantic and southern Africa in ASO are illustrated
204 in Fig. 2a. The atmospheric circulation at 700 hPa is characterised by a continental high centred at

205 25°S over southern Africa and extending over the eastern South Atlantic, and a subtropical trough
206 west of South Africa deflecting the midlatitude westerly flow southward. Massive quantities of BBA
207 are emitted from tropical southern Africa, and are driven westward over the South Atlantic by the
208 southern African easterly jet (Adebiyi and Zuidema, 2016), while the anticyclonic gyre associated
209 with the continental high recirculates the BBA towards South Africa along the Namibian coast. This
210 recirculation merges with smaller BBA amounts emitted from sources located in South Africa in the
211 urban area of Johannesburg and Pretoria, to be eventually transported eastward to the Indian Ocean
212 embedded in the westerly flow.

213 The WR classification shows two synoptic patterns accounting for the oscillation of the pressure field
214 in the South Atlantic and four synoptic patterns accounting for midlatitude pressure anomalies (Fig.
215 4). These four WRs represent the fingerprint of propagative disturbances travelling along the
216 midlatitude mean westerly flow with wave number 8-12, as shown by the EOF analysis (see Section
217 S1). The synoptic variability is dominated by the South Atlantic positive pattern (SA+), which occurs
218 at a frequency of 22.3% and is characterised by a high pressure anomaly in the South Atlantic
219 accompanied by a reinforcement of the midlatitude westerlies (Fig. 4a). Its symmetric counterpart is
220 represented by the South Atlantic negative pattern (SA-), which occurs at a frequency of 17.7% and
221 is characterised by a low pressure anomaly and a weaker westerly flow in the midlatitudes (Fig. 4b).
222 The remaining 60% of the synoptic variability in the region is characterised by eastward travelling
223 disturbances of the westerly flow, represented by midlatitude (ML) anomaly patterns 1-4 (Fig. 4c-f).
224 WR sequences are characterised by short duration, 2-3 days for SA+ and SA-, with extreme
225 persistence values above 10 days; and 1-2 days for ML1-4, with extremes not exceeding 6 days (Fig.
226 5a). The analysis of the WR transitions shows that SA+ and SA- are dominated by persistence (self-
227 transitions are, respectively, 61% and 59% of the total), with reduced transition rates towards the
228 other WRs (Table 2). Conversely, persistence is reduced in the ML patterns (self-transitions are less
229 than 50%), which show non negligible hetero-transition rates (Table 2). Specifically, ML1 shows
230 preference for transitions towards ML2 (28% of the transitions); ML2 prefers transitions towards
231 ML3 (31%); ML3 tends to evolve into ML4 (24%); and ML4 towards ML1 (29%). The transitions of the
232 ML WRs highlight the eastward propagative character of these WRs, suggesting a possible transition
233 pattern from ML1 to ML4 (ML1 → ML2 → ML3 → ML4). The evolution of the atmospheric circulation
234 anomalies from the occurrence of the WR to day +4 is illustrated in Fig. 6. The building and eastward
235 propagation of midlatitude disturbances is evident for ML1-4, which evolve into themselves on day
236 +1 and then into each other on day +2 to +3 (Fig. 6c-f), following the transition pattern ML1 → ML2
237 → ML3 → ML4. This transition pattern depicts the propagation and life cycle of temperate waves
238 embedded in the regional midlatitude dynamics. Conversely, persistence characterises the evolution

239 of SA+ and SA-, evolving into themselves on day +1 to +2, to weaken and disappear on day +3 (Fig.
240 6ab).

241 The sensitivity of the WR classification described above (referred as “control” classification) to
242 different choices of the retained variance (referred as “PC7” classification) and the geographical
243 domain (referred as “shifted” classification) is assessed (see Section S2 for details). Both the “PC7”
244 and “shifted” classifications result in two WRs (SA+ and SA- in Fig. S4) characterised by persistent (2-
245 3 days) pressure anomalies in the South Atlantic (see the analysis of persistence Fig. S5 and
246 transition rates in Tables S1-3) and four WRs (ML1-4 in Fig. S4) characterised by travelling pressure
247 anomalies at the midlatitudes (see Fig. S5 and Tables S1-3), showing no substantial changes in the
248 circulation features identified in “control”. Nevertheless, one ‘spurious’ WR appears in both the
249 modified classifications (ML2 in “PC7” and ML4 in “shifted”), affecting the frequencies of occurrence
250 and the transition rates among WRs (see Fig. S5 and Tables S1-3), and limiting the rate of WR co-
251 occurrence (the fraction of days sharing the same WR with “control”) to 54% in “PC7” and 49% in
252 “shifted”. However, the frequency of the ‘spurious’ WRs is 13% in “PC7” (ML2) and 14% in “shifted”
253 (ML4), and when they are not considered in the computation of the co-occurrence rates, these
254 increase to 72% in “PC7” and 65% in “shifted”. The robustness of the WR classification in the period
255 2003-2017 is also assessed by comparison with the classification of the ASO synoptic variability in
256 the same domain performed on the ERA5 data in the period 1981-2020. The ERA5 classification
257 shows two WRs accounting for pressure anomalies in the South Atlantic, and four WRs accounting
258 for pressure anomalies at the midlatitudes (Fig. 4g-l), characterised by persistence and transitions
259 similar to the CAMS classification (Fig. 5b and Table 3). The comparison of the spatial patterns shows
260 a high degree of similarity between the two classifications, with the WRs almost overlapping in
261 terms of both circulation features and location and intensity of the anomalies (Fig. 4). As expected,
262 the classification in ERA5, performed on a longer time period limiting the influence of the
263 interannual variability, shows reduced differences in the WR frequencies at the seasonal time scale
264 (frequencies are between 13.2% and 19.5% in ERA5 and between 12.1% and 22.3% in CAMS, see Fig.
265 7). The availability of 40 year time series in ERA5 allows to robustly estimate WR frequencies at the
266 intraseasonal time scale (Fig. 7). Differences are limited to 1-2%, with the exception of ML2 and ML3,
267 increasing by 3% and decreasing by 4% during the season, respectively. The comparison of the WR
268 occurrences in the overlapping period (ASO 2003-2017) shows that 81% of the days are
269 characterised by the same WR in ERA5 and CAMS. The sensitivity tests performed on the WR
270 classification of the CAMS data show a high degree of robustness with respect to changes in the time
271 period, and a good degree of robustness with respect to changes in the geographical domain and the

272 retained variance, highlighting that the classification well represents the main features of the
273 synoptic circulation in the region.

274 At the global scale, the variability of the atmospheric circulation south of 20°S is dominated by the
275 southern annular mode (SAM), which consists of out-of-phase surface pressure and geopotential
276 height anomalies between the Antarctic region and the southern midlatitudes, resulting in the
277 modulation of the location and intensity of the westerly wind belt (Baldwin, 2001; Limpasuvan and
278 Hartmann, 1999). The relationship between the WR occurrence and the SAM daily index is
279 investigated applying both the C2E and the E2C approach to the ERA5 classification. When the SAM
280 index is associated with the different WRs, the ANOVA shows that the distributions are not derived
281 from populations with the same mean ($p < 0.01$). However, the C2E characterisation of the SAM index
282 does not show a clear association between positive and negative SAM phases and the WRs (Fig. 8a).
283 When the SAM index quartiles are associated with the changes in the WR frequency (E2C), a
284 significant increase in frequency of SA+ and SA- is detected for large positive values of the SAM
285 index, while large negative values occur when ML1, 3 and 4 are significantly more frequent (Fig. 8b).
286 Not surprisingly, the WRs characterised by travelling midlatitude disturbances are associated with
287 negative SAM phases, i.e. with intensified westerlies. Conversely, positive SAM phases, resulting in
288 weaker westerlies, are associated with increased frequency of the WRs accounting for the pressure
289 anomalies in the South Atlantic.

290 **3.2. Synoptic characterisation of reanalysis aerosol optical depth**

291 The WRs describing propagative disturbances at midlatitudes (ML1-4) are characterised by the
292 longitudinal displacement of high-low pressure anomalies modulating the meridional circulation,
293 which in turn drives the poleward BBA transport above the South Atlantic and southern Africa (Fig.
294 4c-f). In particular, ML3 favours the recirculation of BBA from the ocean towards Namibia and South
295 Africa, leading to significant positive AOD anomalies above all the continental stations (Fig. 4e),
296 while ML2 pushes the BBA recirculation above the South Atlantic and inhibits the BBA transport
297 towards the Indian Ocean (Fig. 4d). Conversely, ML1 and 4 are associated with a weaker BBA
298 transport above Namibia and South Africa, leading to significant negative anomalies above the
299 continental stations, and larger transport towards the Indian Ocean (Fig. 4cf). BBA transport along
300 the Atlantic coast of Namibia and South Africa is also anomalously high during SA-, which is
301 characterised by a low pressure anomaly in the South Atlantic inhibiting the transport towards the
302 subtropical South Atlantic, and leading to significant negative anomalies above Ascension Island, and
303 favouring a poleward route driving anomalous BBA concentrations above the continental stations
304 (Fig. 4b). SA+, characterised by a high pressure anomaly in the South Atlantic strengthening the
305 easterly flow in the Tropics, is the only WR associated with a reinforcement of the main BBA

306 transport route in the tropical South Atlantic, and positive AOD anomalies only affect the Ascension
307 Island station (Fig. 4a).

308 The analysis of persistence and transitions highlights two distinct variability patterns in the WR
309 classification, both developing at synoptic time scales (see Section 3.1). On the one hand, SA+ and
310 SA- are characterised by a pulsating nature, with a lifetime of up to 3 days each (Fig. 6ab), which may
311 affect the variability of the BBA transport in the Tropics. A lead-lag correlation analysis indicates an 8
312 day period for the AOD anomalies to build up in the tropical South Atlantic along the easterly route
313 from tropical Africa (Fig. 9ab). On the other hand, ML1-4 represent the fingerprint of travelling
314 midlatitude disturbances, characterised by up to 2 day persistence and subsequent up to 2 day
315 transitions (Fig. 6c-f), possibly leading the variability of the tropics-extratropics BBA transport. The
316 lead-lag correlation analysis shows a 6 day period for the river of smoke to build up in the South
317 Atlantic and move eastward across southern Africa (Fig. 9cd).

318 **3.3. Synoptic characterisation of aerosol optical depth in-situ observations**

319 The robustness of the synoptic characterisation of the BBA transport obtained from the CAMS data
320 is assessed by linking the WR classification to the observed AOD from AERONET stations in the
321 region. It is highlighted that data availability and coverage in most of the stations is limited (see
322 Table 1), resulting in circa 20-40 observations per WR on average. Only the station in Ascension
323 Island covers the whole period analysed, providing more than 600 observations, i.e. circa 100
324 observations per WR on average.

325 The C2E characterisation of the AOD observations is presented in Fig. 10. AOD anomalies above
326 Ascension Island show significant negative values during SA- (Fig. 10a). The significance of this
327 characterisation is confirmed by the ANOVA with a level of confidence higher than 99%. Just south of
328 the source region in Bonanza, significant positive anomalies are observed during ML4 (Fig. 10b).
329 However, the statistical significance of this characterisation only reaches 93%. AOD variability at the
330 Namibian Stations (Gobabeb, Henties Bay and HESS) is dominated by SA-, leading to significant
331 positive anomalies, and ML1, leading to significant negative anomalies (Fig. 10c-f). In addition,
332 significant positive anomalies are observed in HESS during the occurrence of ML3 (Fig. 10f). The
333 ANOVA supports this characterisation, indicating that the null hypothesis, i.e. that the distributions
334 associated with each WR are derived from populations with the same mean, can be rejected with a
335 level of confidence higher than 99%. Similarly to HESS, the continental station in Upington shows
336 significant negative anomalies during ML1 and 4, and significant positive anomalies during ML3 (Fig.
337 10h), and the ANOVA indicates the rejection of the null hypothesis with 99% level of confidence. In
338 South Africa, the southernmost station in Simon's Town does not show significant anomalies in

339 association with any WR (Fig. 10g), and the ANOVA confirms that the WR classification is not able to
340 characterise the AOD variability ($p=0.09$). The C2E characterisation performed using observed AOD
341 data confirms the relationship between the WRs associated with midlatitude disturbances (ML1, 3
342 and 4) and the BBA transport above the AERONET continental stations, and between SA- and the
343 BBA transport above Ascension Island, as shown by the CAMS data (cf. Fig. 4). The comparison with
344 the synoptic characterisation performed using a 7 cluster classification highlights that the latter is
345 less robust, showing poorer ANOVA performances. Moreover, the additional WR, accounting for a
346 strengthening of the continental high, does not provide further characterisation of the AOD
347 anomalies (see Section S3 for details).

348 The E2C characterisation of the BB AOD station data is presented in Fig. 11. AOD anomalies are
349 divided in quartiles, with quartiles from 1st to 4th representing anomalies from the largest negative
350 to the largest positive, and the relative change in WR occurrence is displayed for each quartile. In
351 Ascension Island, the 3rd quartile is characterised by a significant change in the WR frequency the
352 distribution, with increased occurrence of ML4 (Fig. 11a). The Bonanza station does not show any
353 significant change in the WR occurrence (Fig. 11b). In the Namibian Stations (Gobabeb, Henties Bay
354 and HESS), positive AOD anomalies are associated with significantly more frequent SA- and ML2,
355 while negative anomalies are associated with more frequent ML1 (Fig. 11c-f). In addition, in
356 Gobabeb negative AOD anomalies are also associated with more frequent ML2 and 4 (Fig. 11d); in
357 HESS positive anomalies are also associated with more frequent SA+, ML3 and 4, and negative
358 anomalies are also associated with SA- (Fig. 11f). The South African stations in Upington and Simon's
359 Town show positive AOD anomalies associated with more frequent SA-, ML2 and 3, and negative
360 anomalies associated with more frequent SA-, ML1 and 4 (Fig. 11gh). The E2C characterisation
361 confirms the importance of the midlatitude disturbances in controlling the AOD anomalies at the
362 AERONET continental stations, in particular by driving the largest anomalies (1st and 4th quartiles).
363 However, this approach shows some inconsistencies: ML4, which is characterised by a southerly
364 anomaly in the BBA transport along the Atlantic coast (Fig. 4f), is associated with positive AOD
365 anomalies in HESS instead; similarly SA-, characterised by a northerly BBA transport anomaly along
366 the coast (Fig. 4b), is associated with both positive and negative anomalies in HESS and Upington.
367 The origin of this ambiguities is likely due to the location of these stations at the margin of the BBA
368 transport path associated with the WR circulation patterns, making them highly sensitive to the
369 variability of the circulation around the centroid. The comparison with the synoptic characterisation
370 performed using a 7 class partition highlights the same ambiguities when the AOD anomalies in the
371 continental stations are associated with the WR describing a low pressure anomaly in the South
372 Atlantic (see Section S3 for details).

373 **3.4. Interannual variability**

374 The WR frequency in ASO is also analysed at the interannual time scale, by using the ERA5
375 classification on the period 1981-2020 (Fig. 12). All WRs show similar interannual variability in the
376 frequency of occurrence (3-4% standard deviation) and no trend is found after a Mann-Kendall test
377 at 95% level of confidence is performed. Possible teleconnections controlling the WR interannual
378 variability are analysed by computing the linear correlation between the WR frequency and the SST
379 variability at the global scale (Fig. 13). ML1-4 do not show significant correlation patterns at the
380 global scale (see Fig. S11). Conversely, SA+ and SA- show a relationship with SST anomalies in the
381 tropical Pacific and the North Atlantic. In particular, the occurrence of SA+ is associated with La Niña
382 conditions and cold anomalies in the subtropical North Atlantic (Fig. 13a), while SA- is associated
383 with El Niño conditions and warm anomalies in the subtropical North Atlantic, although the
384 significance of the correlation is reduced (Fig. 13b). The linkage with La Niña conditions can explain
385 the SA+ peak in 2010 (Fig. 12) associated with a strong La Niña event (Boening et al., 2012), and the
386 minimum in 2015 (Fig. 12), associated with an extreme El Niño event (Hu and Fedorov, 2017). The
387 analysis of the WR-SST correlations performed by using NOAA ERSST data show similar
388 teleconnection patterns (Fig. S12). Differently from the WRs associated with travelling disturbances,
389 SA+ and SA- are characterised by short persistence and represent a sort of stationary South Atlantic
390 oscillatory pattern (see Chen, 2014), which might interact with Rossby-wave patterns from the
391 equatorial Pacific during El Niño/Southern Oscillation (ENSO) active phases (e.g. Hoskins and
392 Ambrizzi, 1993). The teleconnection mechanisms are explored by computing the correlation
393 between the WR occurrence and the global geopotential at 200 hPa, the level where teleconnection
394 signals are the strongest. Wave patterns connecting the tropical Pacific to pressure anomalies in the
395 South Atlantic are found for both SA+ and SA-, though significance for SA- is weak (Fig. 13cd). A
396 similar modulation by the ENSO of synoptic regimes in the Southern Hemisphere is also reported
397 during austral summer by Fauchereau et al. (2009) and Pohl et al. (2018). The analysis of the WR-
398 SAM relationship at the interannual time scale shows poor results when the WR frequency time
399 series are correlated with the SAM monthly index. Similarly, the correlation between the WR
400 frequency time series and the monthly averages of the geopotential height at 700 hPa in the
401 Southern Hemisphere does not show evident correlation patterns (not shown).

402 **4. Conclusions**

403 In this paper, the first objective classification of the synoptic circulation over the South Atlantic and
404 southern Africa during the dry season is presented. By using atmospheric circulation data from a
405 reanalysis product, a robust classification with 6 WRs is defined for August-to-October in the period
406 2003-2017. Four WRs (ML1-4) represent the fingerprint of the life cycle of propagative disturbances

407 embedded in the regional midlatitude dynamics, while two WRs (SA+ and SA-) represent the
408 oscillation of the pressure field in the South Atlantic. In particular, SA+ is associated with a reinforced
409 South Atlantic anticyclone, and is the dominant WR during the dry season. The occurrence of ML1-4
410 is favoured by intensified westerlies associated with negative values of the daily SAM index, while
411 SA+ and SA- occurrence is associated with positive SAM phases. All the identified WRs show short
412 persistence, not exceeding 3 days, highlighting the synoptic character of the associated circulation
413 patterns. As a consequence, the analysis of possible teleconnections does not reveal significant
414 remote controls of the WR occurrence at the interannual time scale. Only SA+ and SA-, characterised
415 by slightly longer persistence (up to 3 days), show a weak connection with the El Niño/Southern
416 Oscillation through a tropical-extratropical Rossby wave pattern.

417 The synoptic classification is used to characterise the transport of BBA from equatorial Africa, which
418 dominates the aerosol atmospheric content in the region during the dry season. By analysing
419 reanalysis data, it is found that SA+ and SA- modulate the easterly transport from tropical Africa
420 sources, which is the main climatological transport route. The synoptic characterisation also shows
421 that midlatitude propagative disturbances modulate the BBA transport from equatorial Africa,
422 elucidating the mechanism responsible for the BBA transport to the extratropics, which is peculiar in
423 this period of the year. Specifically, the formation of rivers of smoke is favoured by the low-high
424 pressure anomaly systems characterising the ML WRs, channelling the BBA in the meridional
425 direction (see e.g. ML2 in Fig. 4). Once the river of smoke is formed, it crosses southern Africa
426 embedded in the anomaly pattern travelling eastwards, in turn modulating the AOD anomalies over
427 the continent (see e.g. the ML2 → ML3 → ML4 → ML1 evolution in Fig. 4). The BBA transport
428 characterisation is also tested by using AOD observations from AERONET stations, which show a
429 good degree of consistency with the results based on reanalysis data. However, limited data
430 availability in most of the stations prevents a robust statistical validation of the synoptic
431 characterisation of observations at the regional scale. Results show that the occurrence of ML1 and
432 4 inhibits the BBA transport towards the continental stations (Gobabeb, Henties Bay, HESS and
433 Upington), while ML3 favours the transport above the same locations. Along the Atlantic route, the
434 occurrence of SA- limits the BBA transport towards Ascension Island. In-situ observations in Bonanza
435 and Simon's Town are not well characterised by the WR classification. The former likely because of
436 its proximity to the source region, where emission is not strongly affected by the synoptic
437 atmospheric circulation, the latter possibly because of the poor data coverage.

438 Overall, WR clustering shows to be a valuable tool in discriminating aerosol transport and
439 concentrations over the South Atlantic and southern Africa at the short timescales (day-to-day and
440 synoptic variability). A 7 class partition is also tested for the characterisation of the synoptic

441 variability of the BBA transport. However, this classification does not improve the performance of
442 the 6 class partition, showing overall poorer statistics and not correcting some ambiguities found in
443 the E2C characterisation of the continental AERONET stations.

444 The analysis of the regional circulation patterns controlling the BBA transport the South
445 Atlantic/southern Africa sector is reported in literature mainly as a complement in the discussion of
446 field campaign results. During the SAFARI-92 field experiment, Lindsay et al. (1996) reported
447 pronounced BBA transport across southern Africa towards the Indian Ocean, in association with El
448 Niño conditions and intensified continental high. Conversely, during the SAFARI 2000 campaign
449 (Swap et al., 2003), Stein et al. (2003) found an association between the development of rivers of
450 smoke heading towards the Indian Ocean and increased westerly waves and weaker continental
451 high, concomitant with La Niña conditions (see also Garstang et al., 1996). These contrasting
452 conclusions likely originate from to the limited robustness of the analysis due to the shortness of the
453 observation periods. Based on a longer dataset, the WR characterisation suggest a key role of the
454 westerly waves in controlling the rivers of smoke, supporting the hypothesis of Garstang et al.
455 (1996), although it remains inconclusive concerning the role of ENSO phases.

456 This paper provides new insights in the understanding of the synoptic circulation in the South
457 Atlantic and southern Africa, by characterising for the first time the dry season circulation and the
458 associated rivers of smoke. The characterisation of the transport routes in the region is crucial to
459 support the characterisation of the physical and chemical properties of the BBA, and model the
460 associated impact on clouds and radiation. The WR characterisation is also a valuable resource to
461 develop predictive tools for the BBA spatial distribution in the region. In particular, by using reliable
462 long coverage reanalysis products a classification for past decades can be built, and the BBA spatial
463 distribution can be reconstructed where observations are not available. Furthermore, the WR
464 characterisation can be used in climate model projections to estimate the future evolution of the
465 rivers of smoke in the region.

466 *Data availability.* CAMS data are freely available at the Copernicus Atmospheric Data Store
467 (<https://ads.atmosphere.copernicus.eu/>). AERONET station data are made freely available by the
468 NASA Goddard Space Flight Center (<https://aeronet.gsfc.nasa.gov/>). The SAM daily index is made
469 freely available by the NOAA Climate Prediction Center (<https://www.cpc.ncep.noaa.gov/>).

470 *Supplement.* The supplement related to this article is available online at XXXXXXXXXXXX.

471 *Author contributions.* MG conceived the study, designed and performed the analysis and wrote the
472 paper. BP and MCAC performed the WR classification. All the authors contributed to the discussion
473 and interpretation the results and the writing of the text. PF and CF designed the original AEROCLO-
474 sA observational concept, and co-led the 5-year investigation.

475 *Competing interests.* PF is guest editor for the ACP Special Issue “New observations and related
476 modelling studies of the aerosol–cloud–climate system in the Southeast Atlantic and southern Africa
477 regions”. The remaining authors declare that they have no conflicts of interests.

478 *Special issue statement.* This article is part of the special issue “New observations and related
479 modelling studies of the aerosol–cloud–climate system in the Southeast Atlantic and southern Africa
480 regions (ACP/AMT inter-journal SI)”. It is not associated with a conference.

481 *Acknowledgments.* The authors thank the AERONET PIs (Brent Holben, Nichola Knox, Stuart Piketh,
482 Gillian Maggs-Kollin, Derek Griffith, and Willie Gunter) and their staff for establishing and
483 maintaining the AERONET sites used in this study, and K. Schepanski and F. Waquet for useful
484 discussion. The authors thank two anonymous reviewers for their constructive comments, which
485 helped in improving the quality of the manuscript.

486 *Financial support.* The AEROCLO-sA project was supported by the French National Research Agency
487 under grant agreement n° ANR-15-CE01-0014-01, the French national program LEFE/INSU, the
488 Programme national de Télédétection Spatiale (PNTS, <http://www.insu.cnrs.fr/pnts>), grant n° PNTS-
489 2016-14, the French National Agency for Space Studies (CNES), and the South African National
490 Research Foundation (NRF) under grant UID 105958. The research leading to these results has
491 received funding from the European Union’s 7th Framework Programme (FP7/2014-2018) under
492 EUFAR2 contract n°312609”.

493 **References**

- 494 Abel, S. J., Haywood, J. M., Highwood, E. J., Li, J. and Buseck, P. R.: Evolution of biomass burning
495 aerosol properties from an agricultural fire in southern Africa, *Geophys. Res. Lett.*, 30(15),
496 doi:<https://doi.org/10.1029/2003GL017342>, 2003.
- 497 Adebisi, A. A. and Zuidema, P.: The role of the southern African easterly jet in modifying the
498 southeast Atlantic aerosol and cloud environments, *Q. J. R. Meteorol. Soc.*, 142(697), 1574–1589,
499 doi:10.1002/qj.2765, 2016.
- 500 Adebisi, A. A. and Zuidema, P.: Low Cloud Cover Sensitivity to Biomass-Burning Aerosols and
501 Meteorology over the Southeast Atlantic, *J. Clim.*, 31(11), 4329–4346, doi:10.1175/JCLI-D-17-0406.1,
502 2018.
- 503 Baker, A. R., Lesworth, T., Adams, C., Jickells, T. D. and Ganzeveld, L.: Estimation of atmospheric
504 nutrient inputs to the Atlantic Ocean from 50°N to 50°S based on large-scale field sampling: Fixed
505 nitrogen and dry deposition of phosphorus, *Global Biogeochem. Cycles*, 24(3),
506 doi:<https://doi.org/10.1029/2009GB003634>, 2010.
- 507 Baldwin, M. P.: Annular modes in global daily surface pressure, *Geophys. Res. Lett.*, 28(21), 4115–
508 4118, doi:10.1029/2001GL013564, 2001.
- 509 Barkley, A. E., Prospero, J. M., Mahowald, N., Hamilton, D. S., Popendorf, K. J., Oehlert, A. M.,
510 Pourmand, A., Gatineau, A., Panechou-Pulcherie, K., Blackwelder, P. and Gaston, C. J.: African
511 biomass burning is a substantial source of phosphorus deposition to the Amazon, Tropical Atlantic
512 Ocean, and Southern Ocean, *Proc. Natl. Acad. Sci. U. S. A.*, 116(33), 16216–16221,
513 doi:10.1073/pnas.1906091116, 2019.
- 514 Bellouin, N., Quaas, J., Gryspeerdt, E., Kinne, S., Stier, P., Watson-Parris, D., Boucher, O., Carslaw, K.
515 S., Christensen, M., Daniau, A. -L., Dufresne, J. -L., Feingold, G., Fiedler, S., Forster, P., Gettelman, A.,
516 Haywood, J. M., Lohmann, U., Malavelle, F., Mauritsen, T., McCoy, D. T., Myhre, G., Mülmenstädt, J.,
517 Neubauer, D., Possner, A., Rugenstein, M., Sato, Y., Schulz, M., Schwartz, S. E., Sourdeval, O.,
518 Storelvmo, T., Toll, V., Winker, D. and Stevens, B.: Bounding Global Aerosol Radiative Forcing of
519 Climate Change, *Rev. Geophys.*, 58(1), 1–45, doi:10.1029/2019RG000660, 2020.
- 520 Boening, C., Willis, J. K., Landerer, F. W., Nerem, R. S. and Fasullo, J.: The 2011 La Niña: So strong, the
521 oceans fell, *Geophys. Res. Lett.*, 39(19), n/a-n/a, doi:10.1029/2012GL053055, 2012.
- 522 Chen, G.: Revisit to atmospheric oscillations over global oceans: a combined climatology/modality
523 approach, *Int. J. Climatol.*, 34(8), 2715–2729, doi:<https://doi.org/10.1002/joc.3870>, 2014.
- 524 Crétaf, J., Pohl, B., Dieppoiss, B., Berthou, S. and Pergaud, J.: The Angola Low: relationship with

525 southern African rainfall and ENSO, *Clim. Dyn.*, 52(3–4), 1783–1803, doi:10.1007/s00382-018-4222-
526 3, 2019.

527 Diab, R. D., Jury, M. R., Combrink, J. and Sokolic, F.: A comparison of anticyclone and trough
528 influences on the vertical distribution of ozone and meteorological conditions during SAFARI-92, *J.*
529 *Geophys. Res. Atmos.*, 101(D19), 23809–23821, doi:https://doi.org/10.1029/95JD01844, 1996.

530 Dieppois, B., Pohl, B., Rouault, M., New, M., Lawler, D. and Keenlyside, N.: Interannual to
531 interdecadal variability of winter and summer southern African rainfall, and their teleconnections, *J.*
532 *Geophys. Res. Atmos.*, 121(11), 6215–6239, doi:10.1002/2015JD024576, 2016.

533 Eck, T. F., Holben, B. N., Reid, J. S., Dubovik, O., Smirnov, A., O’Neill, N. T., Slutsker, I. and Kinne, S.:
534 Wavelength dependence of the optical depth of biomass burning, urban, and desert dust aerosols, *J.*
535 *Geophys. Res. Atmos.*, 104(D24), 31333–31349, doi:10.1029/1999JD900923, 1999.

536 Eck, T. F., Holben, B. N., Ward, D. E., Mukelabai, M. M., Dubovik, O., Smirnov, A., Schafer, J. S., Hsu,
537 N. C., Piketh, S. J., Queface, A., Roux, J. Le, Swap, R. J. and Slutsker, I.: Variability of biomass burning
538 aerosol optical characteristics in southern Africa during the SAFARI 2000 dry season campaign and a
539 comparison of single scattering albedo estimates from radiometric measurements, *J. Geophys. Res.*
540 *Atmos.*, 108(D13), doi:https://doi.org/10.1029/2002JD002321, 2003.

541 Fauchereau, N., Pohl, B., Reason, C. J. C., Rouault, M. and Richard, Y.: Recurrent daily OLR patterns in
542 the Southern Africa/Southwest Indian Ocean region, implications for South African rainfall and
543 teleconnections, *Clim. Dyn.*, 32(4), 575–591, doi:10.1007/s00382-008-0426-2, 2009.

544 Flemming, J., Benedetti, A., Inness, A., Engelen, R. J., Jones, L., Huijnen, V., Remy, S., Parrington, M.,
545 Suttie, M., Bozzo, A., Peuch, V.-H., Akritidis, D. and Katragkou, E.: The CAMS interim Reanalysis of
546 Carbon Monoxide, Ozone and Aerosol for 2003–2015, *Atmos. Chem. Phys.*, 17(3), 1945–1983,
547 doi:10.5194/acp-17-1945-2017, 2017.

548 Formenti, P., Elbert, W., Maenhaut, W., Haywood, J., Osborne, S. and Andreae, M. O.: Inorganic and
549 carbonaceous aerosols during the Southern African Regional Science Initiative (SAFARI 2000)
550 experiment: Chemical characteristics, physical properties, and emission data for smoke from African
551 biomass burning, *J. Geophys. Res. Atmos.*, 108(D13), doi:https://doi.org/10.1029/2002JD002408,
552 2003.

553 Formenti, P., D’Anna, B., Flamant, C., Mallet, M., Piketh, S. J., Schepanski, K., Waquet, F., Auriol, F.,
554 Brogniez, G., Burnet, F., Chaboureaud, J.-P., Chauvigné, A., Chazette, P., Denjean, C., Desboeufs, K.,
555 Doussin, J.-F., Elguindi, N., Feuerstein, S., Gaetani, M., Giorio, C., Klopper, D., Mallet, M. D., Nabat, P.,
556 Monod, A., Solmon, F., Namwoonde, A., Chikwililwa, C., Mushi, R., Welton, E. J. and Holben, B.: The

557 Aerosols, Radiation and Clouds in Southern Africa Field Campaign in Namibia: Overview, Illustrative
558 Observations, and Way Forward, *Bull. Am. Meteorol. Soc.*, 100(7), 1277–1298, doi:10.1175/BAMS-D-
559 17-0278.1, 2019.

560 Gao, X., Sorooshian, S., Li, J. and Xu, J.: SST data improve modeling of North American monsoon
561 rainfall, *Eos, Trans. Am. Geophys. Union*, 84(43), 457, doi:10.1029/2003EO430001, 2003.

562 Gao, Y., Yu, S., Sherrell, R. M., Fan, S., Bu, K. and Anderson, J. R.: Particle-Size Distributions and
563 Solubility of Aerosol Iron Over the Antarctic Peninsula During Austral Summer, *J. Geophys. Res.*
564 *Atmos.*, 125(11), e2019JD032082, doi:https://doi.org/10.1029/2019JD032082, 2020.

565 Garstang, M., Tyson, P. D., Swap, R., Edwards, M., Kållberg, P. and Lindesay, J. A.: Horizontal and
566 vertical transport of air over southern Africa, *J. Geophys. Res. Atmos.*, 101(D19), 23721–23736,
567 doi:https://doi.org/10.1029/95JD00844, 1996.

568 Giles, D. M., Sinyuk, A., Sorokin, M. S., Schafer, J. S., Smirnov, A., Slutsker, I., Eck, T. F., Holben, B. N.,
569 Lewis, J., Campbell, J., Welton, E. J., Korokin, S. and Lyapustin, A.: Advancements in the Aerosol
570 Robotic Network (AERONET) Version 3 Database – Automated Near Real-Time Quality
571 Control Algorithm with Improved Cloud Screening for Sun Photometer Aerosol Optical Depth (AOD)
572 Measurements, *Atmos. Meas. Tech. Discuss.*, 1–78, doi:10.5194/amt-2018-272, 2018.

573 Haywood, J. M., Osborne, S. R., Francis, P. N., Keil, A., Formenti, P., Andreae, M. O. and Kaye, P. H.:
574 The mean physical and optical properties of regional haze dominated by biomass burning aerosol
575 measured from the C-130 aircraft during SAFARI 2000, *J. Geophys. Res. Atmos.*, 108(D13), n/a-n/a,
576 doi:10.1029/2002JD002226, 2003.

577 Haywood, J. M., Abel, S. J., Barrett, P. A., Bellouin, N., Blyth, A., Bower, K. N., Brooks, M., Carslaw, K.,
578 Che, H., Coe, H., Cotterell, M. I., Crawford, I., Cui, Z., Davies, N., Dingley, B., Field, P., Formenti, P.,
579 Gordon, H., de Graaf, M., Herbert, R., Johnson, B., Jones, A. C., Langridge, J. M., Malavelle, F.,
580 Partridge, D. G., Peers, F., Redemann, J., Stier, P., Szpek, K., Taylor, J. W., Watson-Parris, D., Wood,
581 R., Wu, H. and Zuidema, P.: The CLOUD–Aerosol–Radiation Interaction and Forcing: Year 2017
582 (CLARIFY-2017) measurement campaign, *Atmos. Chem. Phys.*, 21(2), 1049–1084, doi:10.5194/acp-
583 21-1049-2021, 2021.

584 Hersbach, H., Bell, B., Berrisford, P., Hirahara, S., Horányi, A., Muñoz-Sabater, J., Nicolas, J., Peubey,
585 C., Radu, R., Schepers, D., Simmons, A., Soci, C., Abdalla, S., Abellan, X., Balsamo, G., Bechtold, P.,
586 Biavati, G., Bidlot, J., Bonavita, M., Chiara, G., Dahlgren, P., Dee, D., Diamantakis, M., Dragani, R.,
587 Flemming, J., Forbes, R., Fuentes, M., Geer, A., Haimberger, L., Healy, S., Hogan, R. J., Hólm, E.,
588 Janisková, M., Keeley, S., Laloyaux, P., Lopez, P., Lupu, C., Radnoti, G., Rosnay, P., Rozum, I.,

589 Vamborg, F., Villaume, S. and Thépaut, J.: The ERA5 global reanalysis, *Q. J. R. Meteorol. Soc.*,
590 146(730), 1999–2049, doi:10.1002/qj.3803, 2020.

591 Horowitz, H. M., Garland, R. M., Thatcher, M., Landman, W. A., Dedekind, Z., van der Merwe, J. and
592 Engelbrecht, F. A.: Evaluation of climate model aerosol seasonal and spatial variability over Africa
593 using AERONET, *Atmos. Chem. Phys.*, 17(22), 13999–14023, doi:10.5194/acp-17-13999-2017, 2017.

594 Hoskins, B. J. and Ambrizzi, T.: Rossby Wave Propagation on a Realistic Longitudinally Varying Flow, *J.*
595 *Atmos. Sci.*, 50(12), 1661–1671, doi:10.1175/1520-0469(1993)050<1661:RWPOAR>2.0.CO;2, 1993.

596 Hu, S. and Fedorov, A. V.: The extreme El Niño of 2015-2016 and the end of global warming hiatus,
597 *Geophys. Res. Lett.*, 44(8), 3816–3824, doi:10.1002/2017GL072908, 2017.

598 Huang, B., Thorne, P. W., Banzon, V. F., Boyer, T., Chepurin, G., Lawrimore, J. H., Menne, M. J., Smith,
599 T. M., Vose, R. S. and Zhang, H.-M.: Extended Reconstructed Sea Surface Temperature, Version 5
600 (ERSSTv5): Upgrades, Validations, and Intercomparisons, *J. Clim.*, 30(20), 8179–8205,
601 doi:10.1175/JCLI-D-16-0836.1, 2017.

602 Limpasuvan, V. and Hartmann, D. L.: Eddies and the annular modes of climate variability, *Geophys.*
603 *Res. Lett.*, 26(20), 3133–3136, doi:10.1029/1999GL010478, 1999.

604 Lindsay, J. A., Andreae, M. O., Goldammer, J. G., Harris, G., Annegarn, H. J., Garstang, M., Scholes,
605 R. J. and van Wilgen, B. W.: International geosphere-biosphere programme/international global
606 atmospheric chemistry SAFARI-92 field experiment: Background and overview, *J. Geophys. Res.*
607 *Atmos.*, 101(D19), 23521–23530, doi:10.1029/96JD01512, 1996.

608 Macron, C., Pohl, B., Richard, Y. and Bessafi, M.: How do Tropical Temperate Troughs Form and
609 Develop over Southern Africa?, *J. Clim.*, 27(4), 1633–1647, doi:10.1175/JCLI-D-13-00175.1, 2014.

610 Mallet, M., Solmon, F., Nabat, P., Elguindi, N., Waquet, F., Bouniol, D., Sayer, A. M., Meyer, K.,
611 Roehrig, R., Michou, M., Zuidema, P., Flamant, C., Redemann, J. and Formenti, P.: Direct and semi-
612 direct radiative forcing of biomass-burning aerosols over the southeast Atlantic (SEA) and its
613 sensitivity to absorbing properties: a regional climate modeling study, *Atmos. Chem. Phys.*, 20(21),
614 13191–13216, doi:10.5194/acp-20-13191-2020, 2020.

615 McMillan, W. W., McCourt, M. L., Revercomb, H. E., Knuteson, R. O., Christian, T. J., Doddridge, B. G.,
616 Hobbs, P. V., Lukovich, J. V., Novelli, P. C., Piketh, S. J., Sparling, L., Stein, D., Swap, R. J. and Yokelson,
617 R. J.: Tropospheric carbon monoxide measurements from the Scanning High-Resolution
618 Interferometer Sounder on 7 September 2000 in southern Africa during SAFARI 2000, *J. Geophys.*
619 *Res. Atmos.*, 108(D13), n/a-n/a, doi:10.1029/2002JD002335, 2003.

620 Michelangeli, P. A., Vautard, R. and Legras, B.: Weather regimes: recurrence and quasi stationarity, *J.*

621 Atmos. Sci., 52(8), 1237–1256, doi:10.1175/1520-0469(1995)052<1237:WRRQAQ>2.0.CO;2, 1995.

622 Pistone, K., Redemann, J., Doherty, S., Zuidema, P., Burton, S., Cairns, B., Cochrane, S., Ferrare, R.,
623 Flynn, C., Freitag, S., Howell, S. G., Kacenelenbogen, M., LeBlanc, S., Liu, X., Schmidt, K. S., Sedlacek
624 III, A. J., Segal-Rozenhaimer, M., Shinozuka, Y., Stamnes, S., van Diedenhoven, B., Van Harten, G. and
625 Xu, F.: Intercomparison of biomass burning aerosol optical properties from in situ and remote-
626 sensing instruments in ORACLES-2016, Atmos. Chem. Phys., 19(14), 9181–9208, doi:10.5194/acp-19-
627 9181-2019, 2019.

628 Pohl, B., Dieppois, B., Cr tat, J., Lawler, D. and Rouault, M.: From synoptic to interdecadal variability
629 in southern African rainfall: Toward a unified view across time scales, J. Clim., 31(15), 5845–5872,
630 doi:10.1175/JCLI-D-17-0405.1, 2018.

631 Rayner, N. A., Parker, D. E., Horton, E. B., Folland, C. K., Alexander, L. V., Rowell, D. P., Kent, E. C. and
632 Kaplan, A.: Global analyses of sea surface temperature, sea ice, and night marine air temperature
633 since the late nineteenth century, J. Geophys. Res. Atmos., 108(14), doi:10.1029/2002jd002670,
634 2003.

635 Redemann, J., Wood, R., Zuidema, P., Doherty, S. J., Luna, B., LeBlanc, S. E., Diamond, M. S.,
636 Shinozuka, Y., Chang, I. Y., Ueyama, R., Pfister, L., Ryoo, J.-M., Dobracki, A. N., da Silva, A. M., Longo,
637 K. M., Kacenelenbogen, M. S., Flynn, C. J., Pistone, K., Knox, N. M., Piketh, S. J., Haywood, J. M.,
638 Formenti, P., Mallet, M., Stier, P., Ackerman, A. S., Bauer, S. E., Fridlind, A. M., Carmichael, G. R.,
639 Saide, P. E., Ferrada, G. A., Howell, S. G., Freitag, S., Cairns, B., Holben, B. N., Knobelspiesse, K. D.,
640 Tanelli, S., L’Ecuyer, T. S., Dzambo, A. M., Sy, O. O., McFarquhar, G. M., Poellot, M. R., Gupta, S.,
641 O’Brien, J. R., Nenes, A., Kacarab, M., Wong, J. P. S., Small-Griswold, J. D., Thornhill, K. L., Noone, D.,
642 Podolske, J. R., Schmidt, K. S., Pilewskie, P., Chen, H., Cochrane, S. P., Sedlacek, A. J., Lang, T. J., Stith,
643 E., Segal-Rozenhaimer, M., Ferrare, R. A., Burton, S. P., Hostetler, C. A., Diner, D. J., Seidel, F. C.,
644 Platnick, S. E., Myers, J. S., Meyer, K. G., Spangenberg, D. A., Maring, H. and Gao, L.: An overview of
645 the ORACLES (ObseRvations of Aerosols above CLouds and their intEractionS) project: aerosol–
646 cloud–radiation interactions in the southeast Atlantic basin, Atmos. Chem. Phys., 21(3), 1507–1563,
647 doi:10.5194/acp-21-1507-2021, 2021.

648 Stein, D. C., Swap, R. J., Greco, S., Piketh, S. J., Macko, S. A., Doddridge, B. G., Elias, T. and Brientjes,
649 R. T.: Haze layer characterization and associated meteorological controls along the eastern coastal
650 region of southern Africa, J. Geophys. Res. Atmos., 108(D13), n/a-n/a, doi:10.1029/2002JD003237,
651 2003.

652 Stier, P., Schutgens, N. A. J., Bellouin, N., Bian, H., Boucher, O., Chin, M., Ghan, S., Huneeus, N.,
653 Kinne, S., Lin, G., Ma, X., Myhre, G., Penner, J. E., Randles, C. A., Samset, B., Schulz, M., Takemura, T.,

654 Yu, F., Yu, H. and Zhou, C.: Host model uncertainties in aerosol radiative forcing estimates: Results
655 from the AeroCom Prescribed intercomparison study, *Atmos. Chem. Phys.*, 13(6), 3245–3270,
656 doi:10.5194/acp-13-3245-2013, 2013.

657 von Storch, H. and Zwiers, F. W.: *Statistical Analysis in Climate Research*, Cambridge University Press,
658 Cambridge., 1999.

659 Swap, R., Garstang, M., Macko, S. A., Tyson, P. D., Maenhaut, W., Artaxo, P., Källberg, P. and Talbot,
660 R.: The long-range transport of southern African aerosols to the tropical South Atlantic, *J. Geophys.*
661 *Res. Atmos.*, 101(D19), 23777–23791, doi:10.1029/95JD01049, 1996.

662 Swap, R. J., Annegarn, H. J., Suttles, J. T., King, M. D., Platnick, S., Privette, J. L. and Scholes, R. J.:
663 Africa burning: A thematic analysis of the Southern African Regional Science Initiative (SAFARI 2000),
664 *J. Geophys. Res. Atmos.*, 108(D13), n/a-n/a, doi:10.1029/2003JD003747, 2003.

665 Tang, C., Morel, B., Wild, M., Pohl, B., Abiodun, B. and Bessafi, M.: Numerical simulation of surface
666 solar radiation over Southern Africa. Part 1: Evaluation of regional and global climate models, *Clim.*
667 *Dyn.*, 52(1–2), 457–477, doi:10.1007/s00382-018-4143-1, 2019.

668 Tyson, P. D.: Atmospheric transport of aerosols and trace gases over southern Africa, *Prog. Phys.*
669 *Geogr. Earth Environ.*, 21(1), 79–101, doi:10.1177/030913339702100105, 1997.

670 Vigaud, N., Pohl, B. and Crétat, J.: Tropical-temperate interactions over southern Africa simulated by
671 a regional climate model, *Clim. Dyn.*, 39(12), 2895–2916, doi:10.1007/s00382-012-1314-3, 2012.

672 Wai, K. M., Wu, S., Kumar, A. and Liao, H.: Seasonal variability and long-term evolution of
673 tropospheric composition in the tropics and Southern Hemisphere, *Atmos. Chem. Phys.*, 14(10),
674 4859–4874, doi:10.5194/acp-14-4859-2014, 2014.

675 van der Werf, G. R., Randerson, J. T., Giglio, L., Collatz, G. J., Mu, M., Kasibhatla, P. S., Morton, D. C.,
676 DeFries, R. S., Jin, Y. and van Leeuwen, T. T.: Global fire emissions and the contribution of
677 deforestation, savanna, forest, agricultural, and peat fires (1997–2009), *Atmos. Chem. Phys.*, 10(23),
678 11707–11735, doi:10.5194/acp-10-11707-2010, 2010.

679 van der Werf, G. R., Randerson, J. T., Giglio, L., van Leeuwen, T. T., Chen, Y., Rogers, B. M., Mu, M.,
680 van Marle, M. J. E., Morton, D. C., Collatz, G. J., Yokelson, R. J. and Kasibhatla, P. S.: Global fire
681 emissions estimates during 1997–2016, *Earth Syst. Sci. Data*, 9(2), 697–720, doi:10.5194/essd-9-697-
682 2017, 2017.

683 Wu, H., Taylor, J. W., Szpek, K., Langridge, J. M., Williams, P. I., Flynn, M., Allan, J. D., Abel, S. J., Pitt,
684 J., Cotterell, M. I., Fox, C., Davies, N. W., Haywood, J. and Coe, H.: Vertical variability of the
685 properties of highly aged biomass burning aerosol transported over the southeast Atlantic during

686 CLARIFY-2017, *Atmos. Chem. Phys.*, 20(21), 12697–12719, doi:10.5194/acp-20-12697-2020, 2020.

687 Zuidema, P., Chang, P., Medeiros, B., Kirtman, B. P., Mechoso, R., Schneider, E. K., Toniazzo, T.,
688 Richter, I., Small, R. J., Bellomo, K., Brandt, P., De Szoeki, S., Farrar, J. T., Jung, E., Kato, S., Li, M.,
689 Patricola, C., Wang, Z., Wood, R. and Xu, Z.: Challenges and prospects for reducing coupled climate
690 model sst biases in the eastern tropical atlantic and pacific oceans: The U.S. Clivar eastern tropical
691 oceans synthesis working group, *Bull. Am. Meteorol. Soc.*, 97(12), 2305–2327, doi:10.1175/BAMS-D-
692 15-00274.1, 2016.

693

Table 1. AERONET station used in this study: locations and data availability (Version 3 Direct Sun algorithm, level2).

Station	Country	Latitude	Longitude	Observations (coverage)
Ascension Island (AI)	UK Overseas Territory	8.0°S	14.4°W	612 (2003-2017)
Bonanza (BO)	Namibia	21.8°S	19.6°E	126 (2016-2017)
Namibian Stations (NS)	Namibia			276 (2013-2017)
Gobabeb (GO)	Namibia	23.6°S	15.0°E	219 (2015-2017)
Henties Bay (HB)	Namibia	22.1°S	14.3°E	139 (2013-2017)
HESS (HE)	Namibia	23.3°S	16.5°E	158 (2016-2017)
Simon's Town IMT (ST)	South Africa	34.2°S	18.4°E	127 (2016-2017)
Upington (UP)	South Africa	28.4°S	21.2°E	111 (2015-2016)

Table 2. WR transition rates in the CAMS classification, computed as the percentage of transitions from a WR (rows) towards the others (columns). By definition, the diagonal represents persistence. Transition rates above 1/6, i.e. the threshold for non-random transitions, are reported in bold.

WR	SA+	SA-	ML1	ML2	ML3	ML4
SA+	61	6	6	11	6	8
SA-	10	59	5	10	8	7
ML1	8	14	39	28	8	3
ML2	12	5	3	46	31	2
ML3	12	9	4	6	45	24
ML4	12	13	29	3	3	40

Table 3. WR transition rates in the ERA5 classification, computed as the percentage of transitions from a WR (rows) towards the others (columns). By definition, the diagonal represents persistence. Transition rates above 1/6, i.e. the threshold for non-random transitions, are reported in bold.

WR	SA+	SA-	ML1	ML2	ML3	ML4
SA+	58	8	4	13	6	10
SA-	7	60	9	10	8	6
ML1	7	18	42	21	8	4
ML2	11	5	3	50	27	3
ML3	4	12	6	4	45	28
ML4	14	7	23	5	5	46

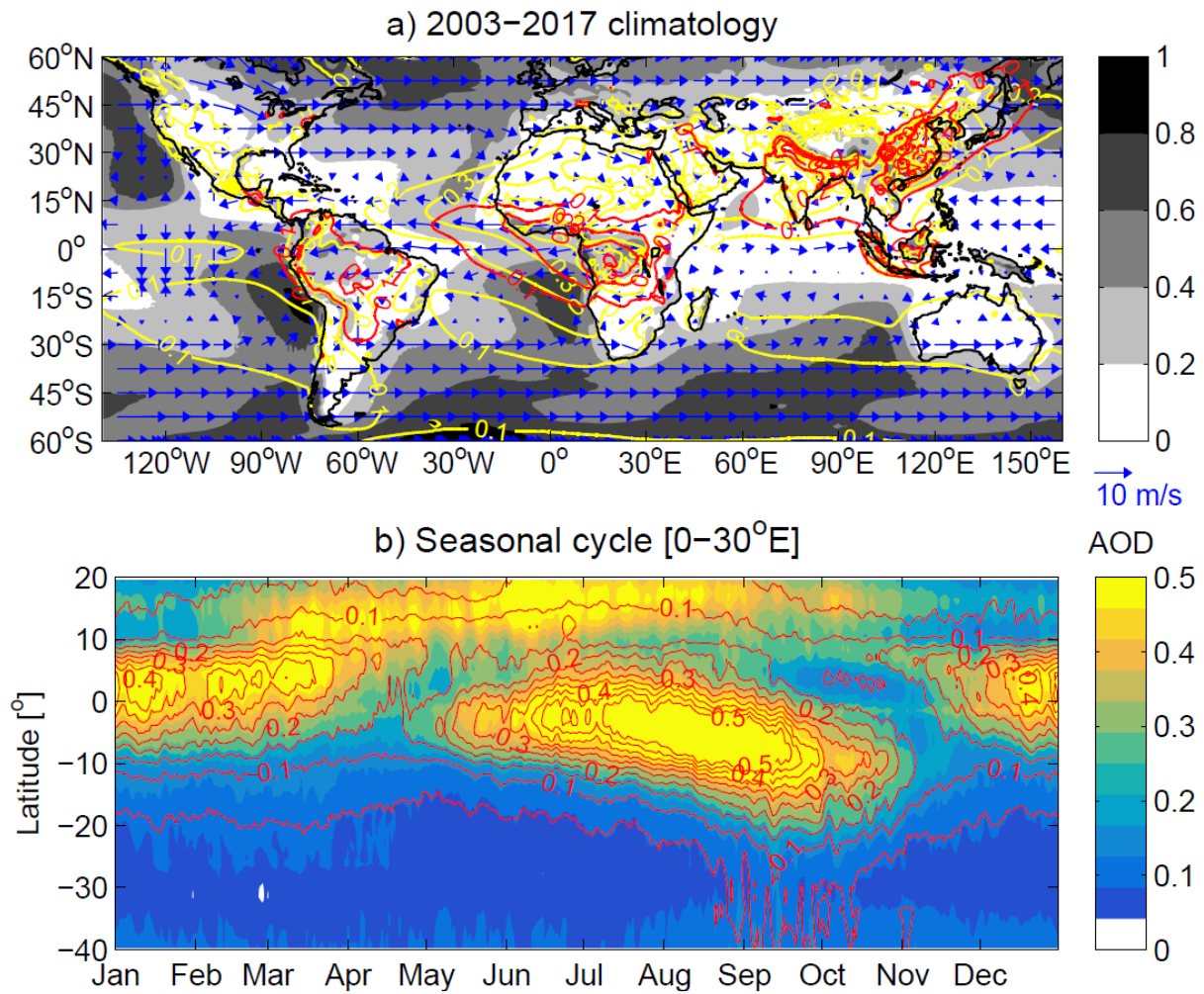


Figure 1. 2003–2017 climatology derived from CAMS reanalysis: (a) annual mean of total (yellow contours) and organic matter (red contours) aerosol optical depth (AOD) at 550 nm, low cloud cover fraction (shadings) and wind at 700 hPa (arrows); (b) annual cycle of total (shadings) and organic matter (red contours) AOD at 550 nm, averaged over Africa and South Atlantic [0–30°E].

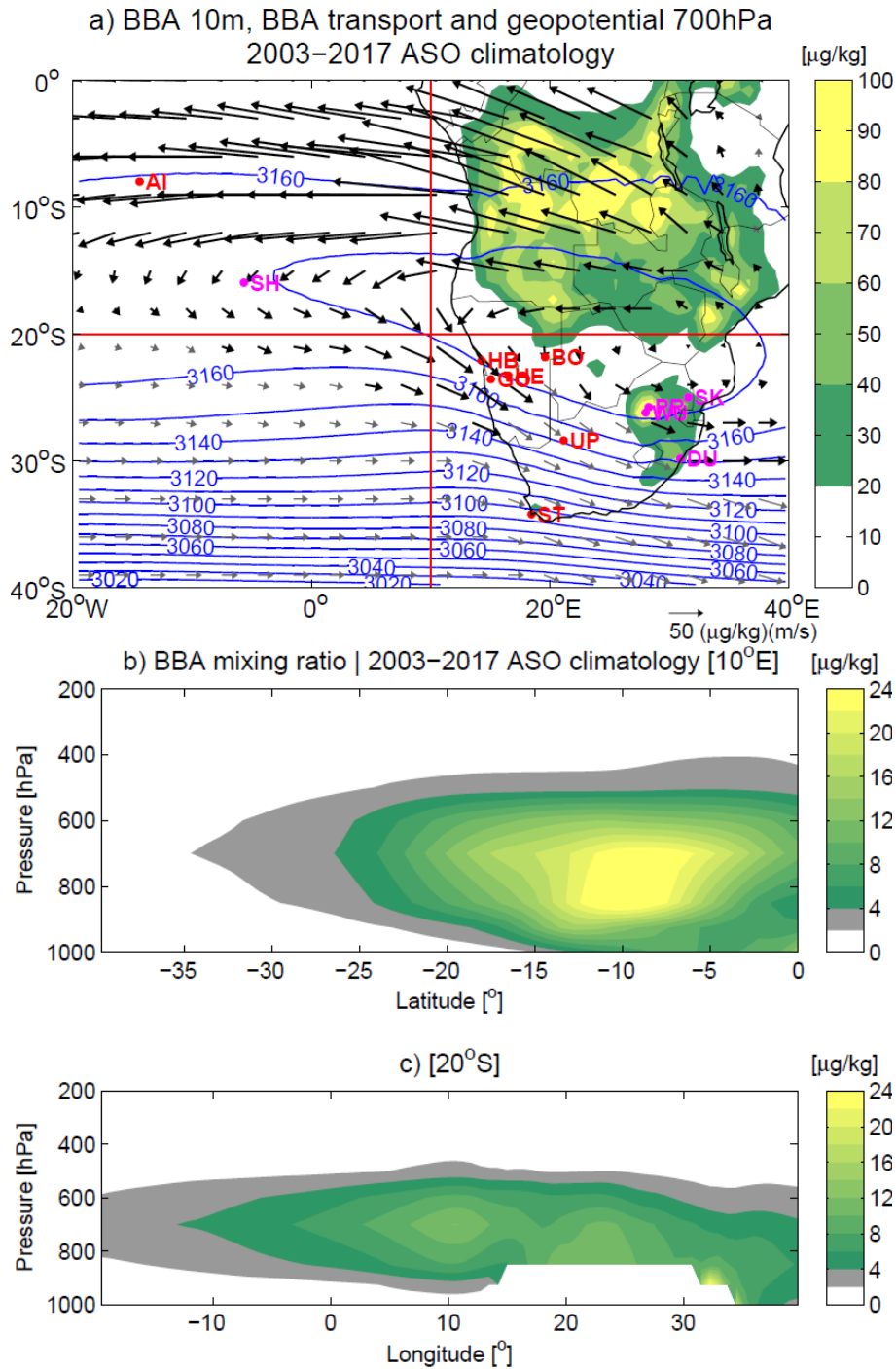


Figure 2. 2003–2017 ASO climatology derived from CAMS reanalysis: (a) organic matter mixing ratio at 10m ($\mu\text{g}/\text{kg}$, shadings), organic matter transport at 700 hPa ($\mu\text{g}/\text{kg m/s}$, arrows) and geopotential height at 700 hPa (m, contours); vertical cross-sections of the organic matter mixing ratio ($\mu\text{g}/\text{kg}$) at (b) 0°E and (c) 25°S . In (a), thick arrows highlight organic matter transport corresponding to organic matter mixing ratio greater than $4 \mu\text{g}/\text{kg}$; red lines indicate where organic matter mixing ratio cross-sections are computed; red dots indicate the locations of the AERONET stations used in this study (see Table 1 for details); magenta dots indicate the locations of available stations not used in this study (see Section 2.2 for details).

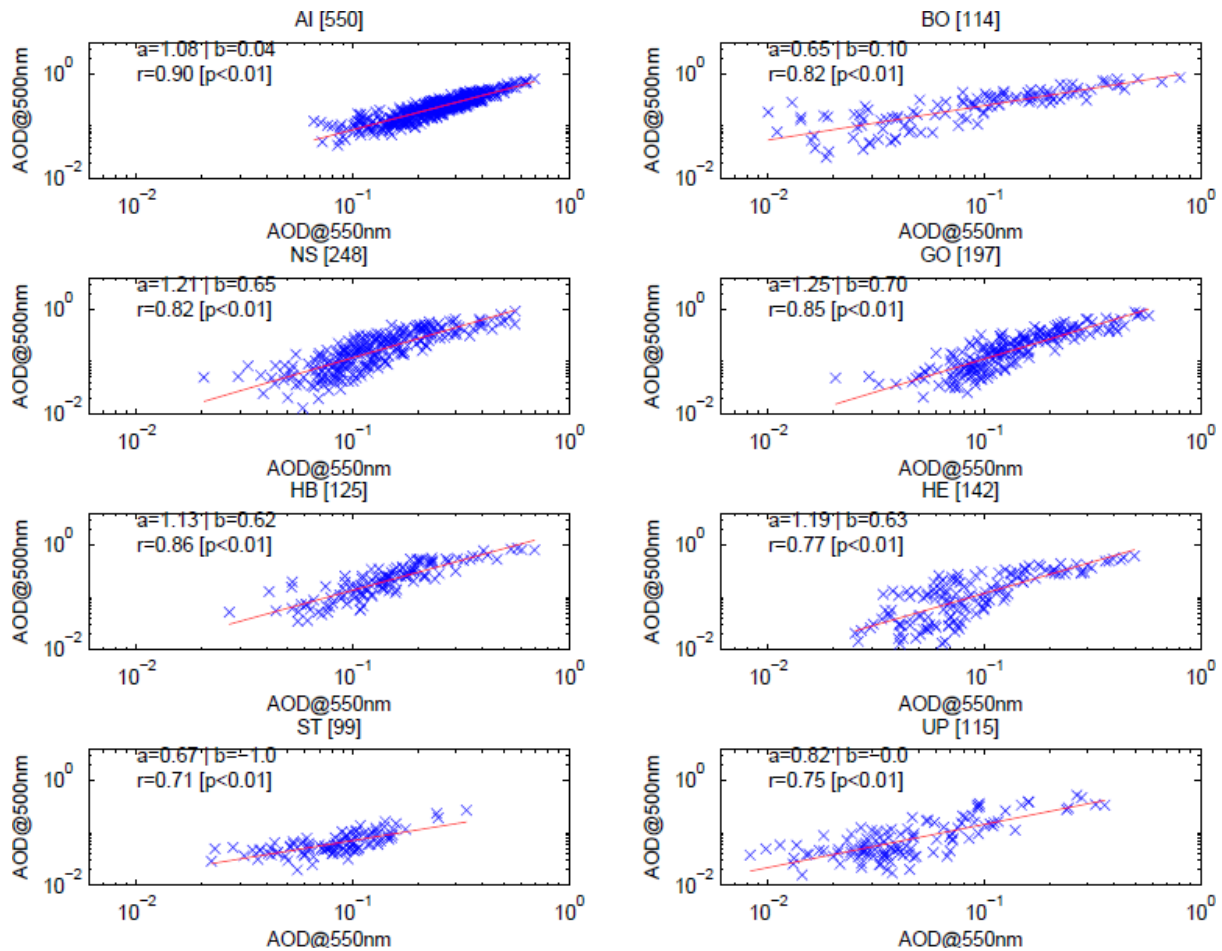


Figure 3. Daily data comparison for ASO 2003-2017: CAMS reanalysis AOD at 550 nm vs AERONET observed AOD at 500 nm. CAMS data are extracted at grid points the closest to the station coordinates (see Table 1). Red lines display the linear regression between CAMS and AERONET data, and the coefficients of the regression models are also reported in the plots, along with the correlation coefficient and the p-value. In titles, the size of the sample used in the linear regression model is reported in brackets (see Section 2.2 for details).

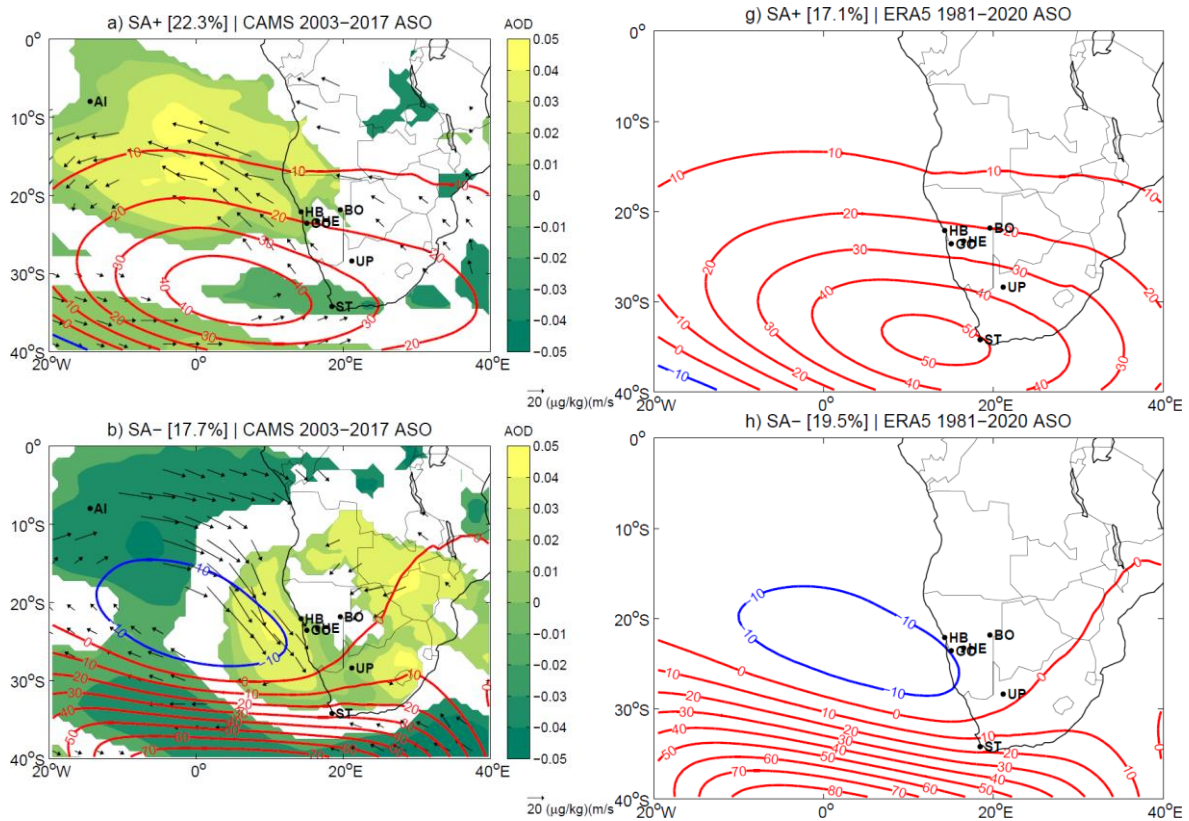


Figure 4. Left panels: anomaly patterns of CAMS geopotential height (m, contours), AOD at 550 nm (shadings) and organic matter transport ($(\mu\text{g}/\text{kg})(\text{m}/\text{s})$, arrows) at 700 hPa associated with the WRs classified from CAMS geopotential height at 700 hPa in ASO 2003-2017. Right panels: anomaly patterns of ERA5 geopotential height (m, contours) at 700 hPa associated with the WRs classified from ERA5 geopotential height at 700 hPa in ASO 1981-2020. Dots indicate the locations of the AERONET stations used in this study. Frequency of the WRs is indicated in brackets. For AOD and organic matter transport, only values significant at 95% level of confidence after a Student's t-test are displayed.

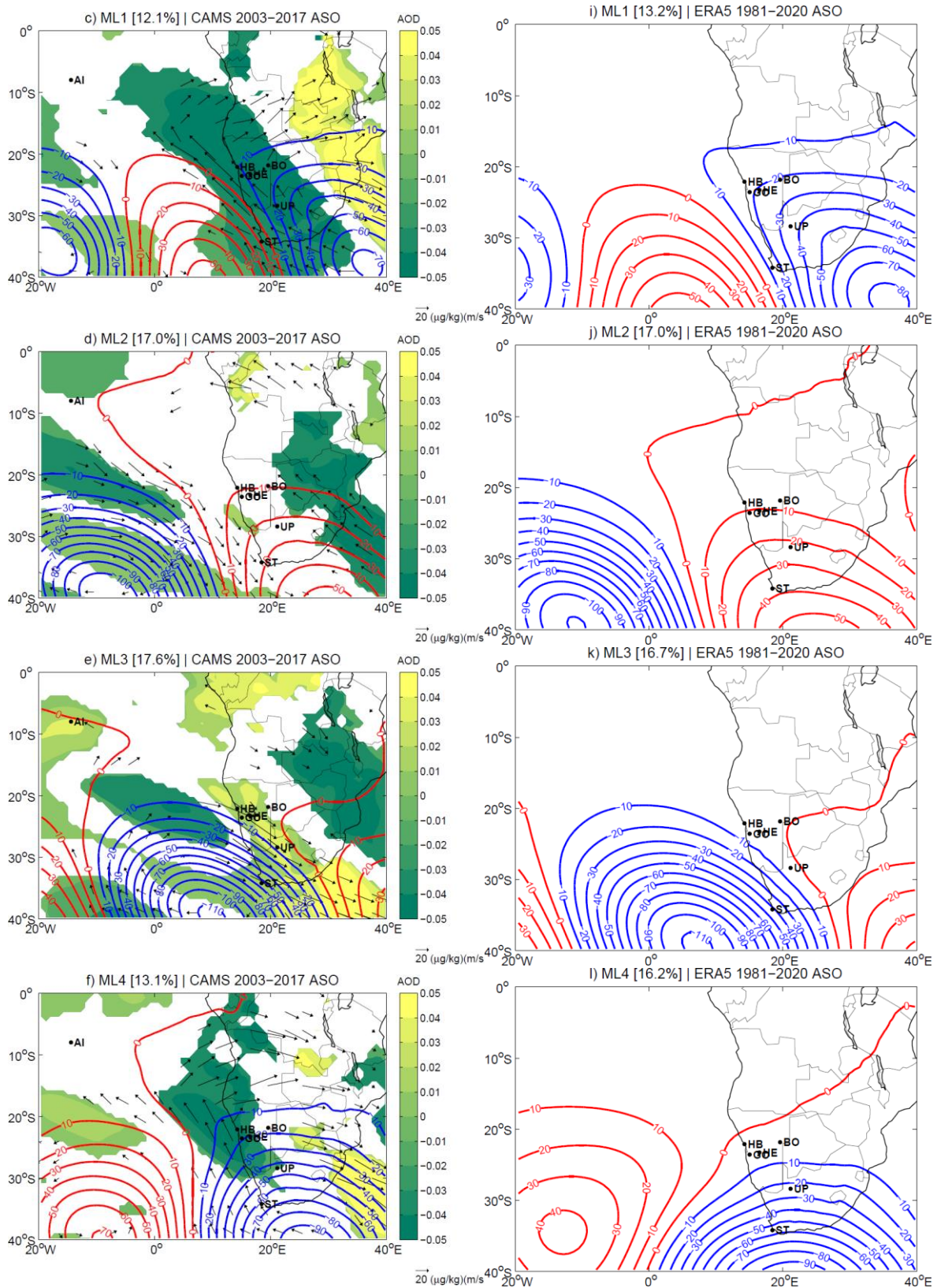


Figure 4. Continued.

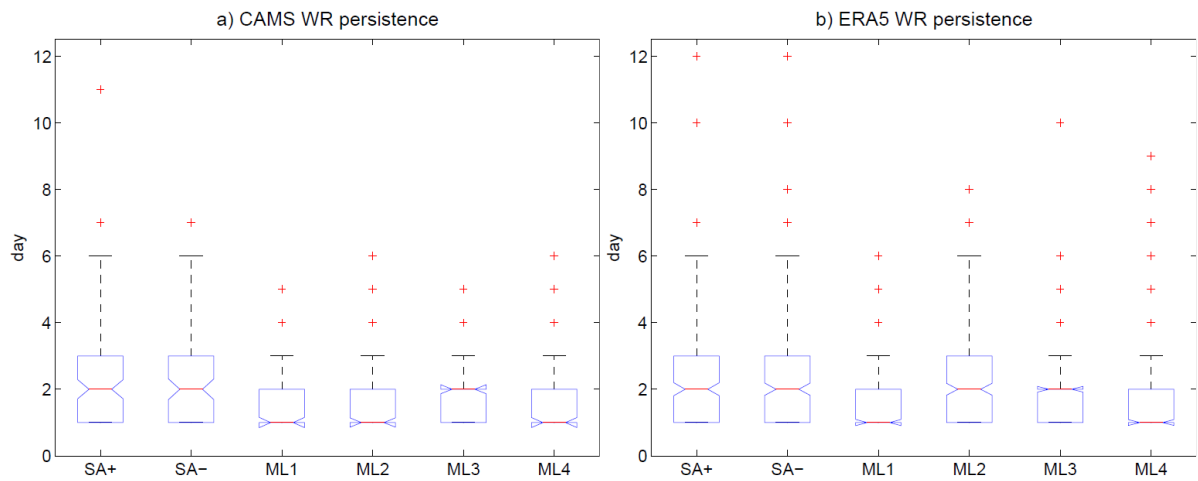


Figure 5. WR persistence in (a) CAMS and (b) ERA5 classifications, displayed as the distribution of the WR sequences. Red lines represent the median, boxes represent the interquartile range, whiskers extend up to the 1.5 of the interquartile range, outliers are displayed as red crosses.

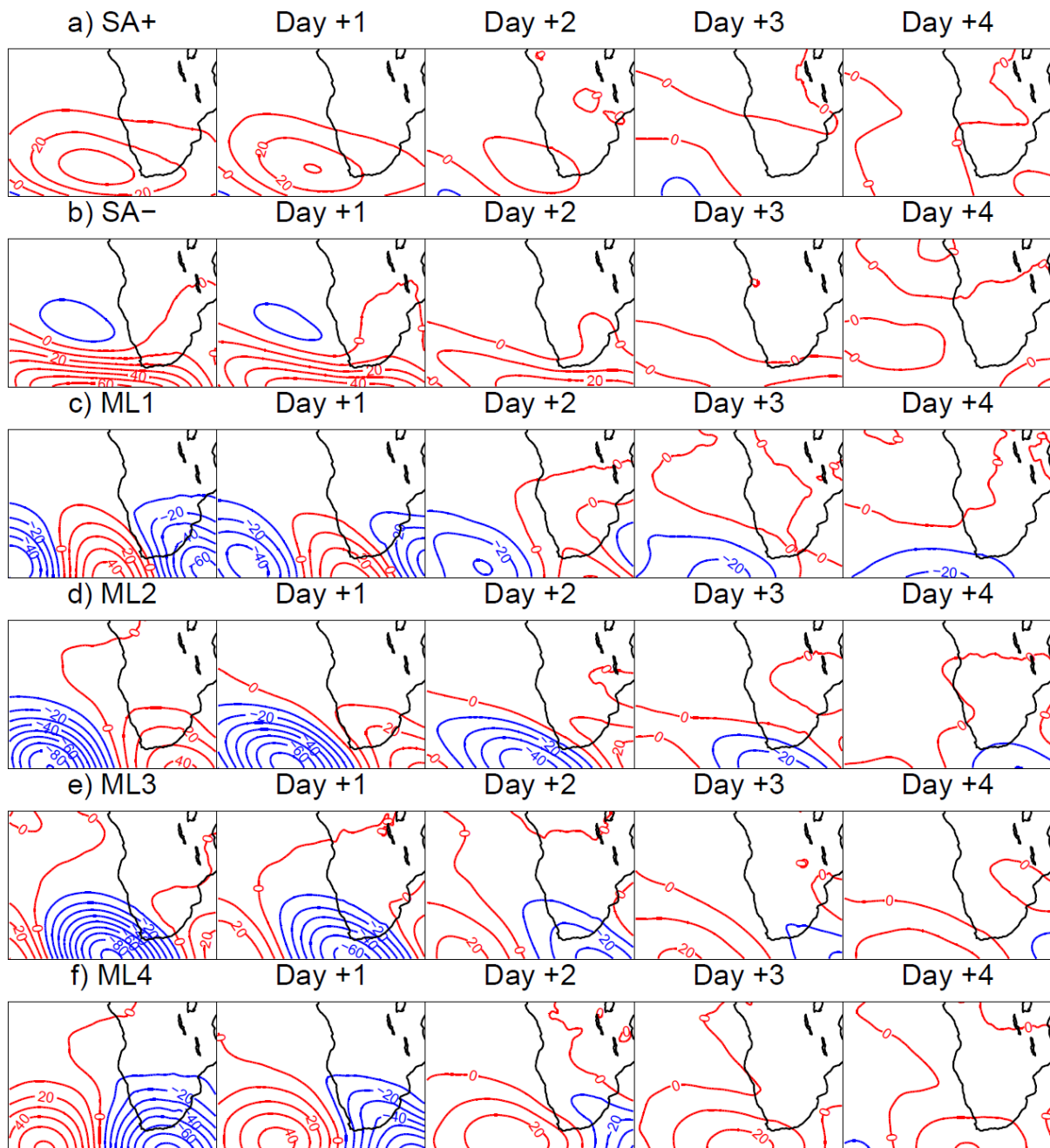


Figure 6. Daily evolution of the 700 hPa geopotential height anomalies (m, contours) associated with the CAMS WR classification, computed as composites from the WR occurrence (day 0) to day +4.

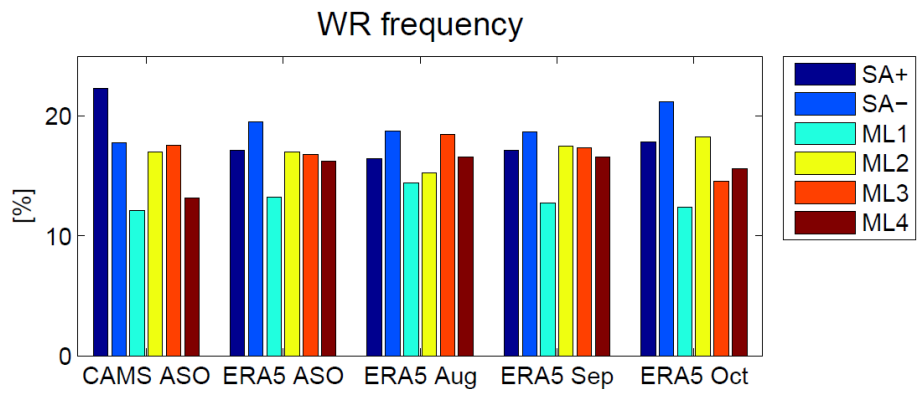


Figure 7. WR frequency in CAMS (computed in the period 2003-2017) and ERA5 (computed in the period 1981-2020) classifications.

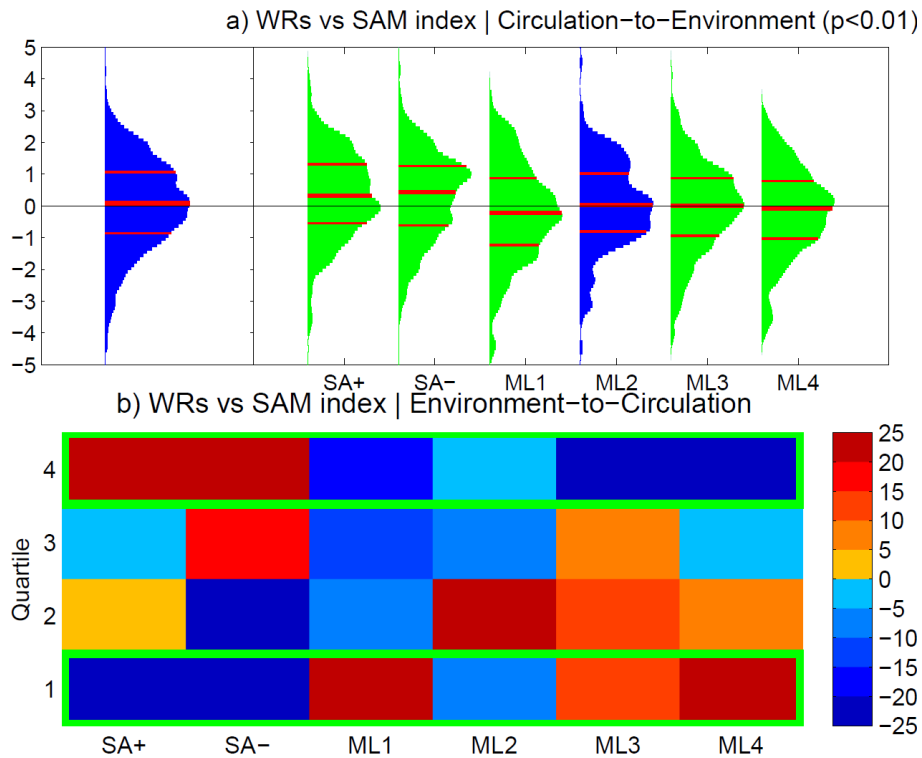


Figure 8. (a) Circulation to environment characterisation (C2E): (left panel) daily Southern Annular Model (SAM) index distribution, and (right panel) for each ERA5 WR. Probability density functions are estimated by using a normal kernel density; red lines represent 25th, 50th and 75th percentiles. Anomaly distributions significantly different from the climatological sample are displayed in green (significance is assessed by a Kolmogorov-Smirnov test at 95% level of confidence). The p-value of the ANOVA used to assess the C2E characterisation is reported in brackets. (b) Environment to circulation characterisation (E2C): ERA5 WR frequency anomaly for each quartile of the daily SAM index. Values represent percentage changes relative to climatological frequencies. Green boxes highlight significant changes in the WR frequencies, i.e. frequency anomalies exceeding the critical threshold (11.07) for the chi-squared statistics with 5 degrees of freedom at 95% level of confidence (see Section 2.4 for details).

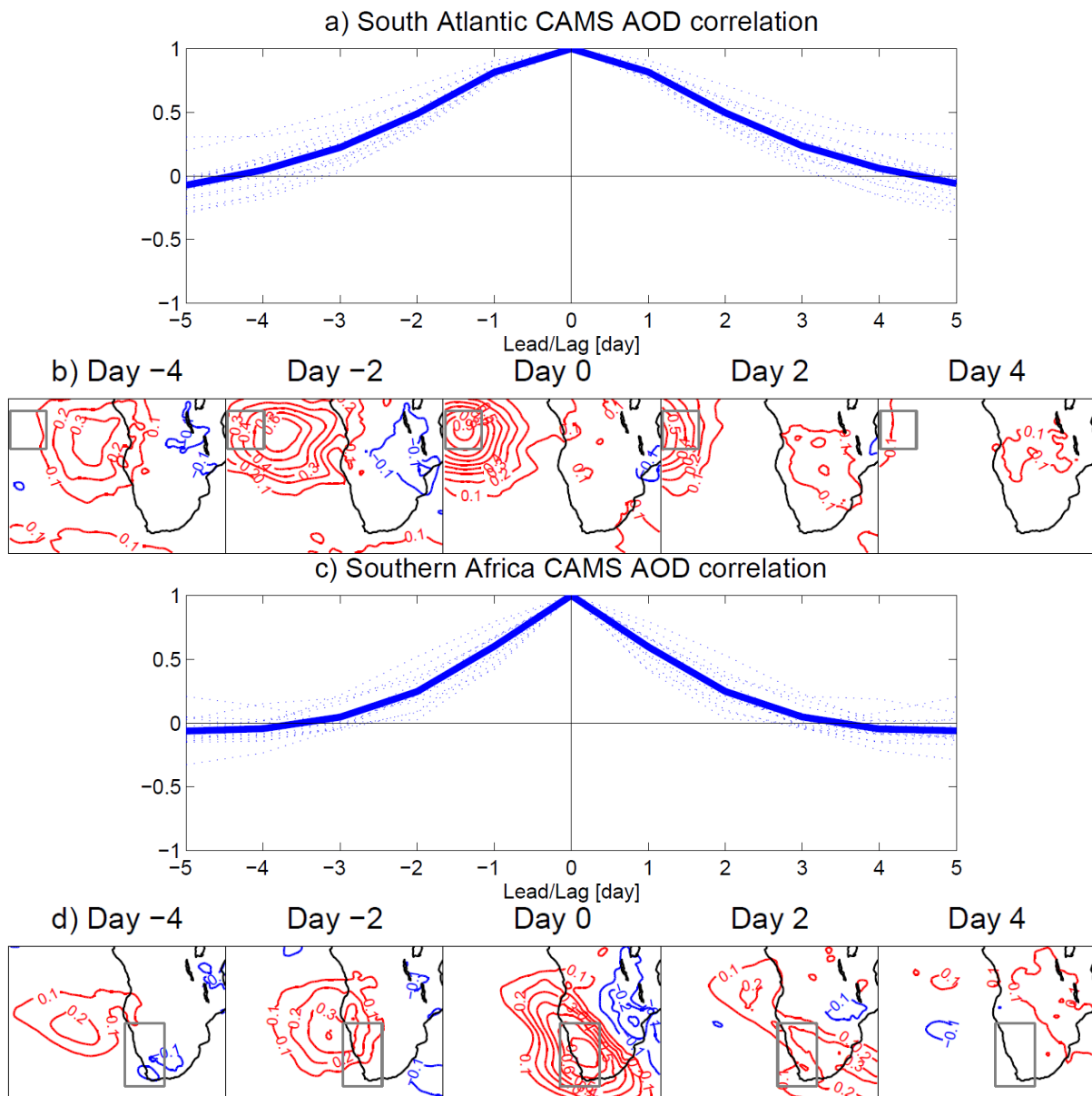


Figure 9. Daily lead-lag correlation analysis of CAMS AOD anomalies. AOD anomalies averaged in the (a) South Atlantic and (c) southern Africa are correlated with themselves: dotted lines display individual year correlations; South Atlantic and southern Africa domains are displayed as boxes in (b) and (d), respectively. Correlation maps: AOD anomalies averaged in the (b) South Atlantic and (d) southern Africa are correlated with the AOD anomalies in the South Atlantic/southern Africa domain. Correlations are computed year-by-year and averaged.

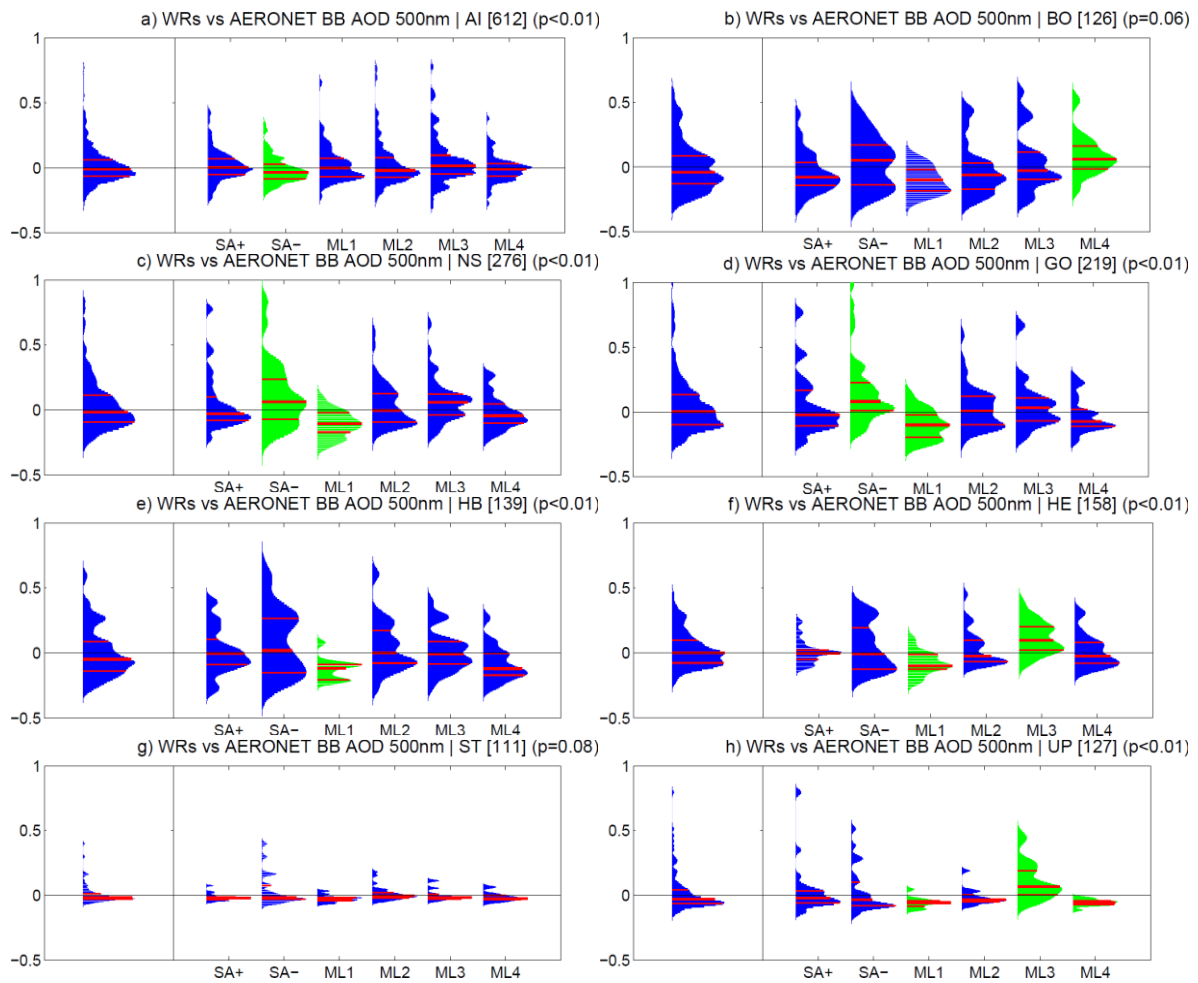


Figure 10. Circulation to environment characterisation: for each AERONET station, (left panel) distribution of the AOD anomalies at 500 nm, and (right panel) for each CAMS WR. Probability density functions are estimated by using a normal kernel density; red lines represent 25th, 50th and 75th percentiles. Anomaly distributions significantly different from the climatological sample are displayed in green (p -values of the Kolmogorov-Smirnov test used to assess the significance of the differences are reported in Table S5). In titles, the number of available daily observations and the p -value of the ANOVA used to assess the WR characterisation are reported in brackets.

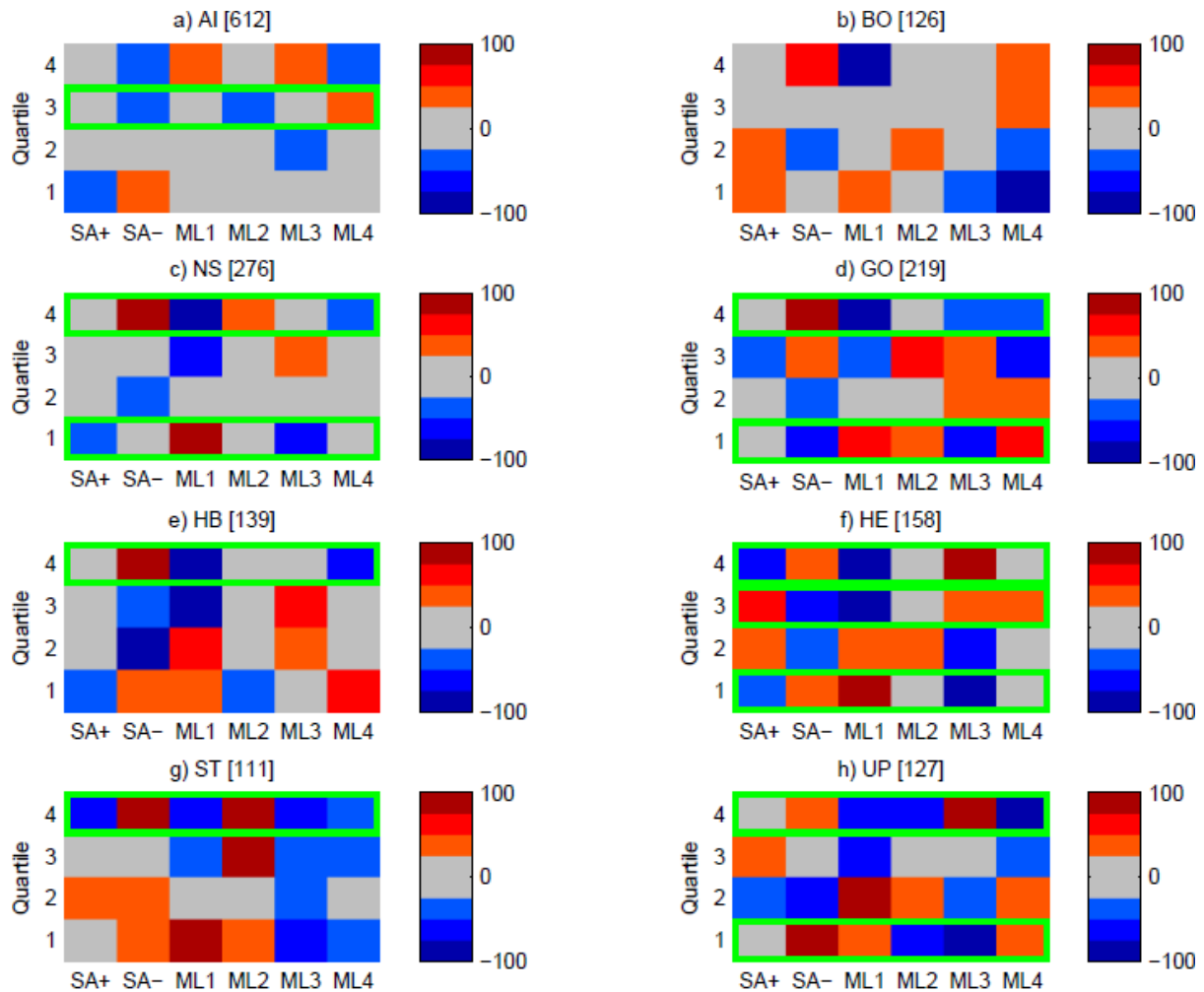


Figure 11. Environment to circulation characterisation: CAMS WR frequency anomaly for each quartile of the AOD anomalies at 500 nm at the AERONET stations. Values represent percentage changes relative to climatological frequencies. Green boxes highlight significant changes in the WR frequencies, i.e. frequency anomalies exceeding the critical threshold (11.07) for the chi-squared statistics with 5 degrees of freedom at 95% level of confidence (chi-squared statistics are reported in Table S6). In brackets, the number of available daily observations are indicated.

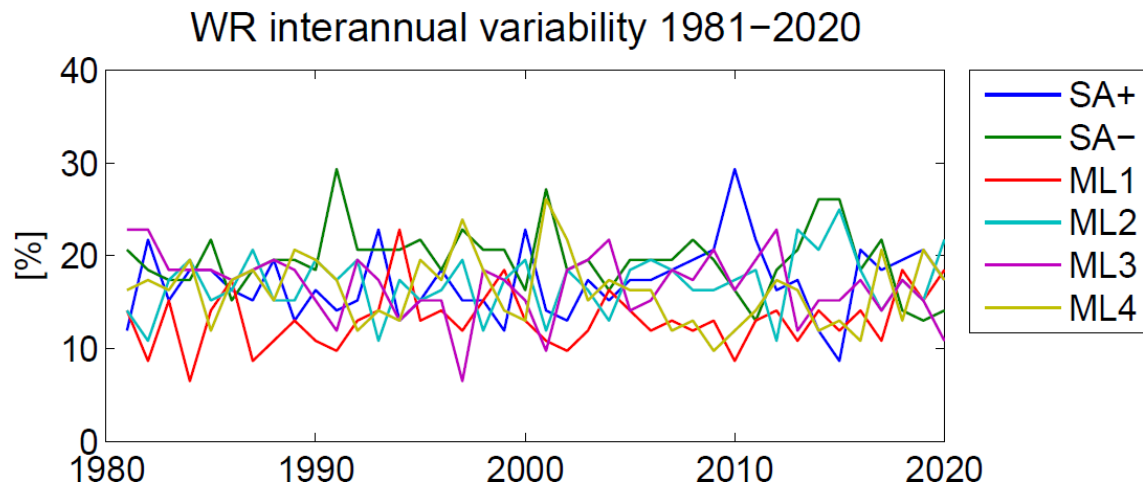


Figure 12. ERA5 WR frequency 1981-2020: interannual variability.

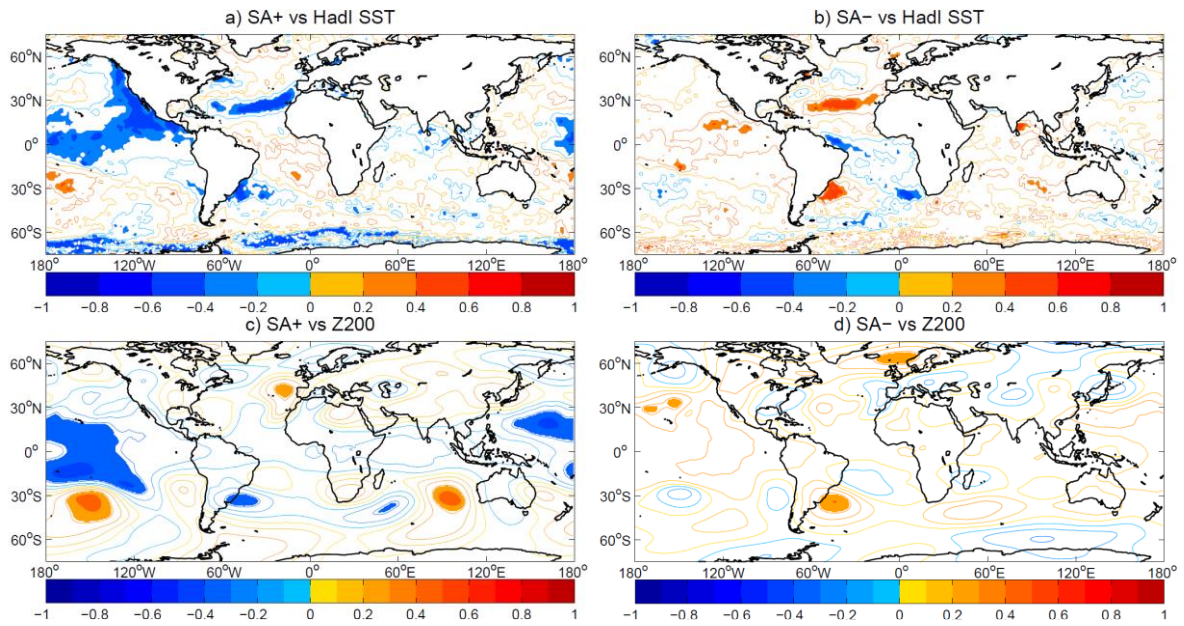


Figure 13. Interannual correlation over the period 1981-2020: SA+ and SA- frequency from the ERA5 classification vs (a, b) Hadl sea surface temperature and (c, d) ERA5 geopotential height at 200 hPa in ASO. Shadings display significant correlations at 95% level of confidence. Time series are detrended and standardised.